Properties of the mean momentum balance in turbulent Taylor–Couette flow

Tie Wei†

Department of Mechanical Engineering, New Mexico Institute of Mining and Technology, Socorro, NM 87801, USA

This paper investigates the properties of the mean momentum balance (MMB) equation in the azimuthal ϕ direction of a turbulent Taylor–Couette flow (TCF). The MMB-ϕ equation is integrated to determine the properties of the Reynolds shear stress. An approximation is developed for the Reynolds shear stress in the core region of a turbulent TCF, and the dependence of the peak Reynolds shear stress location on the Reynolds number and the gap geometry is revealed. The properties of the global integral of the turbulent Coriolis force are also revealed. For a turbulent TCF with a small gap or at high Reynolds numbers, the global integral of the turbulent Coriolis force is found to be only weakly influenced by the rotation ratio of the cylinders. Two controlling non-dimensional numbers are derived directly from the scaling analysis of the MMB-ϕ equation. The first is a geometry Atwood number $A_t \overset{\text{def}}{=} \delta/r_{ctr}$ to characterize the gap geometry, where δ is the gap half-width, and r_{ctr} is the mid-gap radial location. The second is the friction Reynolds number $Re_{\tau,i}$ defined as $Re_{\tau,i} \overset{\text{def}}{=} \delta u_{\tau,i}/\nu$, where ν is the kinematic viscosity and $u_{\tau,i}$ is the friction velocity at the inner cylinder. A new three-layer structure is proposed for the inner half of a turbulent TCF at sufficiently high Reynolds number, based on the force balance in the MMB-ϕ equation. Layer I is an inner layer, where the force balance is between the viscous force and the Reynolds shear force: $F_{visc} \approx -F_{turb}$. Layer III occupies the core of the gap, where the force balance is between the turbulent Coriolis force and the Reynolds shear force: $F_{cori} \approx -F_{turb}$. In Layer II, all three forces contribute to the balance. An inner scaling is developed for Layer I, and an outer scaling is developed for Layer III. The inner and outer scalings are verified against direct numerical simulation data. Similarities and differences between the turbulent TCF and a pressure-driven turbulent channel flow are elucidated.

Key words: Taylor–Couette flow

1. Introduction

Rotating flow in the gap between two concentric cylinders, commonly known as Taylor–Couette flow (TCF), is a classic example of a simple system with complex and rich stability properties. On the practical side, TCF occurs in astrophysical

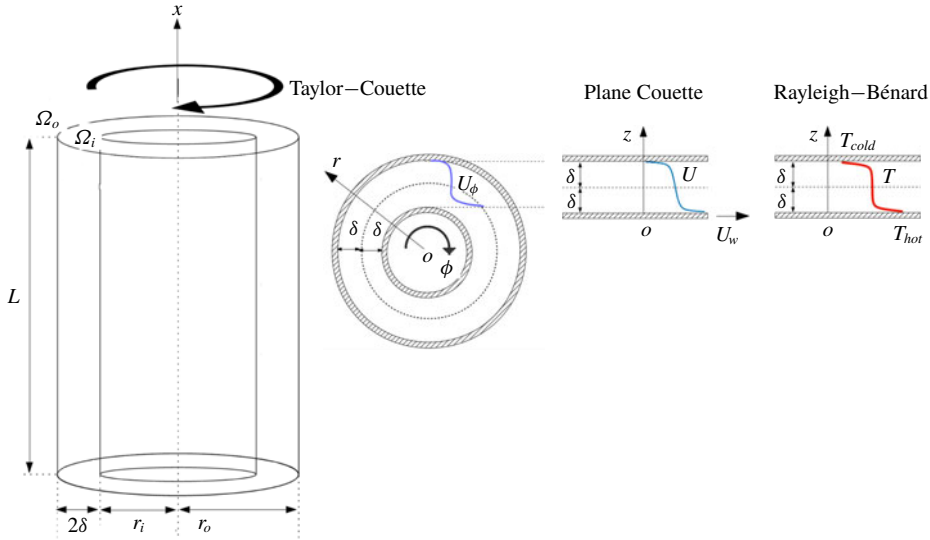† Email address for correspondence: tie.wei@nmt.edu

FIGURE 1. Geometry and coordinate system of a Taylor–Couette flow. The inner and outer cylinders can rotate in either direction, independently. Also shown are plane Couette flow and Rayleigh–Bénard convection. Gap half-width is denoted as $\delta = 0.5(r_o - r_i)$, analogous to the channel half-height in PCF, or half-height in RBC.

accretion discs, turbines and journal bearings. Flow in the gap between two concentric cylinders was first studied by Couette (1890) and Mallock (1896). The history of early developments in the area is given by Donnelly (1991). A tutorial review of TCF is given by Fardin, Perge & Taberlet (2014). A recent review paper by Grossmann, Lohse & Sun (2016) lists research areas of particular current interest in TCF including instability, nonlinear dynamics, spatio-temporal chaos, pattern formation and turbulence. While TCF has been well studied, however, much remains to be learned about the physics involved.

As sketched in figure 1, TCF is controlled by six parameters: the kinematic viscosity of the fluid ν, the inner cylinder radius r_i, the outer cylinder radius r_o, the cylinder height L, the angular velocity of the inner cylinder Ω_i and that of the outer cylinder Ω_o. Dimensional analysis suggests that TCF is governed by four non-dimensional numbers, and a variety of forms have been proposed for defining the non-dimensional numbers, especially the Reynolds number. One commonly used set of non-dimensional numbers is

$$\Pi_1 = \Pi_r \overset{\text{def}}{=} \frac{r_i}{r_o}; \tag{1.1a}$$

$$\Pi_2 = \Gamma \overset{\text{def}}{=} \frac{L}{2\delta}; \tag{1.1b}$$

$$\Pi_3 = Re_i \overset{\text{def}}{=} \frac{(r_o - r_i)r_i|\Omega_i|}{\nu}; \tag{1.1c}$$

$$\Pi_4 = \Pi_\Omega \overset{\text{def}}{=} \frac{\Omega_i}{\Omega_o}. \tag{1.1d}$$

For brevity, the gap half-width is denoted as $\delta = 0.5(r_o - r_i)$, analogous to the channel half-width in a plane Couette flow (PCF) or the half-height in a Rayleigh–Bénard

convection (RBC) cell. The first non-dimensional number Π_1 is a measure of the gap geometry; Π_2 is a measure of the gap height to its width, commonly called the aspect ratio Γ; Π_3 is a definition of the Reynolds number; Π_4 is a measure of the relative rotation of the two cylinders; $\Pi_\Omega = 0$ is the special case in which only the outer cylinder rotates and $\Pi_\Omega = \infty$ is the special case in which only the inner cylinder rotates; $\Pi_\Omega < 0$ is counter-rotating and $\Pi_\Omega > 0$ is co-rotating.

Dubrulle *et al.* (2005) introduced an alternative set of non-dimensional control parameters, based on dynamic rather than geometric considerations. The development of these new control parameters was motivated by the need to compare flows that do not share identical geometry. For a TCF, Dubrulle *et al.* (2005) chose the gap width 2δ as the unit length, the inverse of a typical shear S as the unit time and $\sqrt{r_i r_o}$ as a typical radius.

Over the past three decades, TCF has been extensively studied experimentally by several research groups, including, for example, Professor Egbers's group at Brandenburg University of Technology Cottbus-Senftenberg (see Merbold, Brauckmann & Egbers 2013), Professor Lathrop's group at the University of Maryland (see Zimmerman, Triana & Lathrop 2011), Professor Lohse's group at the University of Twente (see van Gils *et al.* 2011), Professor Mutabazi's group at the Université du Havre (see Martínez-Arias *et al.* 2014), Professor Swinney's group at the University of Austin (see Andereck, Liu & Swinney 1986) and Professor Westerweel's group at Delft University of Technology (see Ravelet, Delfos & Westerweel 2010). Their experimental studies have greatly increased our understanding of various aspects of TCF, developed important experimental methods and provided important data sets.

Over the past twenty years, and in particular the past ten years, direct numerical simulation (DNS) has become an important tool in the investigation of TCF. The Reynolds number range achievable in DNS is still lower than that in experimental studies, but DNS can provide detailed data on flows that are challenging to measure experimentally. The analysis in the present work requires the second-order spatial derivative of the mean velocity and the first-order spatial derivative of the Reynolds shear stress, and DNS offers the high resolution and high accuracy to compute those derivatives. Here, several DNS studies are briefly reviewed to provide the simulation parameters and their main findings.

Dong (2007) simulated a TCF system with $r_i/r_o = 0.5$ and the outer cylinder fixed, covering four Reynolds numbers: $Re_i = (2\delta r_i |\Omega_i|)/\nu = 1000, 3000, 5000, 8000$. Dong (2007) reported the average axial spacing of the streaks caused by Görtler vortices, and presented flow dynamics and statistics. Dong (2008) simulated a counter-rotating TCF system with $r_i/r_o = 0.5$ and documented the statistical features in detail. Dong (2008) demonstrated the effects of the Coriolis force on the mean flow between the standard TCF system (rotating inner cylinder and fixed outer cylinder) and the counter-rotating TCF system.

Pirro & Quadrio (2008) simulated a small-gap TCF with the outer cylinder at rest. In their simulation, the friction Reynolds number based on the friction velocity at the inner cylinder $u_{\tau,i}$ is $Re_{\tau,i} \overset{\text{def}}{=} \delta u_{\tau,i}/\nu = 189.3$ for the inner cylinder half and the friction Reynolds number based on the friction velocity at the outer cylinder $u_{\tau,o}$ is $Re_{\tau,o} \overset{\text{def}}{=} \delta u_{\tau,o}/\nu = 167.7$ for the outer cylinder half. They reported the profiles of the mean azimuthal velocity, and the variance of velocity fluctuations in the radial, azimuthal and axial directions.

Ostilla–Monico and collaborators (Ostilla-Mónico *et al.* 2013, 2014; Ostilla-Mónico, Verzicco & Lohse 2015) have performed extensive DNS studies to examine the effect of computational domain size and radial ratio. To save simulation time, some of

their simulations used a quarter of the domain, employing rotational symmetry of order four (Ostilla-Mónico *et al.* 2013). They examined the mean and fluctuation velocities, as well as autocorrelations and velocity spectra. The smallest domain size was found to accurately reproduce the torque and mean azimuthal velocity profiles of the larger domain, but produced smaller values of fluctuations than the larger domain size simulation.

Brauckmann & Eckhardt (2013) performed DNS of TCF using a spectral code with periodic boundary conditions in the axial direction and aspect ratio $\Gamma = 2$. They found a maximum in the angular velocity transport for the counter-rotation with $-\Omega_o/\Omega_i \approx 0.4$. Tanaka, Kawata & Tsukahara (2018) performed a series of simulations of a counter-rotating TCF system with relatively small radius ratios $r_i/r_o = 0.2$–0.5. They investigated the effect of radius ratio on the flow state. Tanaka *et al.* (2018) observed that at small radius ratio, the Reynolds shear stress on the outer side remained approximately zero, but the intensity of the velocity fluctuations was comparable to that of the Taylor-vortex flow in the central region.

DNS data have been used to explore various aspects of TCF. However, a systematic scaling analysis of the mean momentum balance equation in TCF is still lacking, and this is the motivation of the present work. The rest of this paper is organized as follows. In § 2, the governing equations of the TCF are presented. For a fully developed turbulent TCF, the Reynolds averaged equations in the radial and azimuthal directions are presented. The properties of the Reynolds shear stress and the turbulent Coriolis force are revealed by integrating the mean momentum equation. In § 3, a layer structure is proposed for a turbulent TCF based on the characteristics of the force balance. The scaling analysis leads to new non-dimensional numbers for Π_1 and Π_3. An outer scaling and an inner scaling are developed for the outer layer and inner layer, respectively. In § 4, the limitations of the analysis, along with areas for future investigation, are discussed. Section 5 summarizes the work.

2. Governing equations

The continuity equation and Navier–Stokes equations in a cylindrical coordinate system are (Townsend 1980; Landau & Lifshitz 1987; Schlichting & Gersten 2016)

$$0 = \frac{\partial \tilde{u}_r}{\partial r} + \frac{\tilde{u}_r}{r} + \frac{1}{r}\frac{\partial \tilde{u}_\phi}{\partial \phi} + \frac{\partial \tilde{u}_x}{\partial x}; \quad \text{Continuity} \tag{2.1a}$$

$$\begin{aligned} \frac{\partial \tilde{u}_r}{\partial t} &+ \frac{\partial(\tilde{u}_r\tilde{u}_r)}{\partial r} + \frac{1}{r}\frac{\partial(\tilde{u}_\phi\tilde{u}_r)}{\partial \phi} + \frac{\partial(\tilde{u}_x\tilde{u}_r)}{\partial x} + \frac{\tilde{u}_r\tilde{u}_r - \tilde{u}_\phi\tilde{u}_\phi}{r} \\ &= -\frac{\partial}{\partial r}\left(\frac{\tilde{p}}{\rho}\right) + \nu\left\{\frac{\partial^2\tilde{u}_r}{\partial r^2} + \frac{1}{r}\frac{\partial \tilde{u}_r}{\partial r} - \frac{\tilde{u}_r}{r^2} + \frac{1}{r^2}\frac{\partial^2\tilde{u}_r}{\partial \phi^2} + \frac{\partial^2\tilde{u}_r}{\partial x^2} - \frac{2}{r^2}\frac{\partial \tilde{u}_\phi}{\partial \phi}\right\}; \quad \text{NS-}r \end{aligned} \tag{2.1b}$$

$$\begin{aligned} \frac{\partial \tilde{u}_\phi}{\partial t} &+ \frac{\partial(\tilde{u}_r\tilde{u}_\phi)}{\partial r} + \frac{1}{r}\frac{\partial(\tilde{u}_\phi\tilde{u}_\phi)}{\partial \phi} + \frac{\partial(\tilde{u}_x\tilde{u}_\phi)}{\partial x} + \frac{2\tilde{u}_r\tilde{u}_\phi}{r} \\ &= -\frac{1}{r}\frac{\partial}{\partial \phi}\left(\frac{\tilde{p}}{\rho}\right) + \nu\left\{\frac{\partial^2\tilde{u}_\phi}{\partial r^2} + \frac{1}{r}\frac{\partial \tilde{u}_\phi}{\partial r} - \frac{\tilde{u}_\phi}{r^2} + \frac{1}{r^2}\frac{\partial^2\tilde{u}_\phi}{\partial \phi^2} + \frac{\partial^2\tilde{u}_\phi}{\partial x^2} + \frac{2}{r^2}\frac{\partial \tilde{u}_r}{\partial \phi}\right\}; \quad \text{NS-}\phi \end{aligned} \tag{2.1c}$$

$$\begin{aligned} \frac{\partial \tilde{u}_x}{\partial t} &+ \frac{\partial(\tilde{u}_r\tilde{u}_x)}{\partial r} + \frac{1}{r}\frac{\partial(\tilde{u}_\phi\tilde{u}_x)}{\partial \phi} + \frac{\partial(\tilde{u}_x\tilde{u}_x)}{\partial x} + \frac{\tilde{u}_r\tilde{u}_x}{r} \\ &= -\frac{\partial}{\partial x}\left(\frac{\tilde{p}}{\rho}\right) + \nu\left\{\frac{\partial^2\tilde{u}_x}{\partial r^2} + \frac{1}{r}\frac{\partial \tilde{u}_x}{\partial r} + \frac{1}{r^2}\frac{\partial^2\tilde{u}_x}{\partial \phi^2} + \frac{\partial^2\tilde{u}_x}{\partial x^2}\right\}. \quad \text{NS-}x \end{aligned} \tag{2.1d}$$

Here, r is the radial direction, ϕ is the azimuthal direction and x is the axial direction; ρ is the fluid density. Note that the continuity (2.1a) is used to present the momentum equations (2.1b)–(2.1d) in a conservation form, for the convenience of performing the Reynolds averaging operation. In the present work, the instantaneous variable is denoted by a tilde, an upper case letter denotes its mean and a lower case letter denotes its fluctuation. For example, in $\tilde{u}_\phi = U_\phi + u_\phi$, $\tilde{u}_\phi$ is the instantaneous azimuthal velocity, U_ϕ is the mean azimuthal velocity and u_ϕ is the azimuthal velocity fluctuation.

The present work assumes that the turbulent TCF is statistically homogeneous in the axial x direction. In other words, it is assumed that the height of the cylinders is much larger than the gap width or $\Gamma \gg 10$ (see Chouippe *et al.* 2014). For a fully developed turbulent TCF, the only non-zero component of mean velocity is in the azimuthal ϕ direction, and the mean values depend only on the radial location: $U_r = U_x = 0$, $\partial/\partial\phi = 0$ and $\partial/\partial x = 0$ (Townsend 1980).

For Navier–Stokes equations in a cylindrical coordinate system, the viscous shear stress is (see Taylor 1936; Landau & Lifshitz 1987)

$$\tau_{r\phi} = \mu \left(\frac{1}{r} \frac{\partial U_r}{\partial \phi} + \frac{\partial U_\phi}{\partial r} - \frac{U_\phi}{r} \right). \tag{2.2}$$

For a fully developed turbulent TCF, the first term on the right side of (2.2) is zero. In the present work, the positive ϕ direction is defined such that dU_ϕ/dr is negative. For example, if only the inner cylinder is rotating, the positive azimuthal direction is the direction of rotation. If only the outer cylinder is rotating, the positive azimuthal direction is the direction opposite the direction of rotation. Under such a coordinate system, the mean azimuthal velocity decreases in the radial direction and the Reynolds shear stress is negative.

Using the convention commonly followed for turbulent wall-bounded flows (see Tennekes & Lumley 1972), the friction velocities at the inner cylinder and outer cylinder, respectively, are defined as

$$u_{\tau,i} \overset{\text{def}}{=} \sqrt{\frac{|\tau_{r\phi}|_{r=r_i}}{\rho}} = \sqrt{\nu \left| \frac{dU_\phi}{dr} - \frac{U_\phi}{r} \right|_{r=r_i}}; \tag{2.3a}$$

$$u_{\tau,o} \overset{\text{def}}{=} \sqrt{\frac{|\tau_{r\phi}|_{r=r_o}}{\rho}} = \sqrt{\nu \left| \frac{dU_\phi}{dr} - \frac{U_\phi}{r} \right|_{r=r_o}}. \tag{2.3b}$$

The moment (or torque) at the inner cylinder is $M_i = (2\pi r L \tau_{r\phi} r)_{r=r_i}$, and the moment (or torque) at the outer cylinder is $M_o = (2\pi r L \tau_{r\phi} r)_{r=r_o}$. Substituting the definitions of the friction velocities in (2.3a) and (2.3b), the moment at the inner cylinder can be expressed as $|M_i| = 2\pi r_i^2 L \rho u_{\tau,i}^2$, and the moment at the outer cylinder can be expressed as $|M_o| = 2\pi r_o^2 L \rho u_{\tau,o}^2$.

For a TCF system in a statistical steady state, global moment (or torque) balance, analogous to the force balance in a plane Couette flow, dictates $M_i = -M_o$ or

$$2\pi r_i^2 L \rho u_{\tau,i}^2 = 2\pi r_o^2 L \rho u_{\tau,o}^2. \tag{2.4}$$

Hence, the friction velocity at the inner cylinder and outer cylinder are related to each other as

$$\frac{u_{\tau,i}}{u_{\tau,o}} = \frac{r_o}{r_i}. \tag{2.5}$$

Therefore, the wall shear stress or friction velocity at the inner cylinder is always larger than at the outer cylinder, regardless of which cylinder is rotating or the rotation ratio. In the sketch of mean azimuthal velocity in figure 1, the velocity profile is steeper near the inner cylinder than near the outer cylinder.

For a steady state turbulent TCF, Reynolds averaging is both time averaging and plane averaging in the ϕ–x plane. Applying Reynolds averaging, the mean momentum balance equation in the r direction (MMB-r) and ϕ direction (MMB-ϕ) can be expressed as

$$0 = \underbrace{-\frac{\mathrm{d}}{\mathrm{d}r}\left(\frac{P}{\rho}\right)}_{F_{pres}} + \underbrace{\frac{\mathrm{d}R_{rr}}{\mathrm{d}r}}_{F_{turb\text{-}r}} + \underbrace{\frac{U_\phi U_\phi + R_{rr} - R_{\phi\phi}}{r}}_{F_{cent}}; \quad \text{MMB-}r \tag{2.6a}$$

$$0 = \underbrace{\nu\left\{\frac{\mathrm{d}^2 U_\phi}{\mathrm{d}r^2} + \frac{1}{r}\frac{\mathrm{d}U_\phi}{\mathrm{d}r} - \frac{U_\phi}{r^2}\right\}}_{F_{visc}} + \underbrace{\frac{\mathrm{d}R_{r\phi}}{\mathrm{d}r}}_{F_{turb\text{-}\phi}} + \underbrace{\frac{2R_{r\phi}}{r}}_{F_{cori}}, \quad \text{MMB-}\phi \tag{2.6b}$$

where $R_{rr} = -\langle u_r u_r \rangle$ and $R_{\phi\phi} = -\langle u_\phi u_\phi \rangle$ are the kinematic Reynolds normal stresses in the r and ϕ directions, respectively. Here, $R_{r\phi} = -\langle u_r u_\phi \rangle$ is the kinematic Reynolds shear stress. Angle brackets $\langle \rangle$ denote Reynolds averaging.

The MMB-r equation (2.6a) represents the balance of three forces in the radial r direction: a pressure force F_{pres}, a Reynolds normal force $F_{turb\text{-}r}$ and a centrifugal force F_{cent}. The pressure force and the Reynolds normal forces are analogous to those in the wall-normal direction of a turbulent pipe or channel flow. The centrifugal force consists of two parts: one from the mean flow $(U_\phi U_\phi)/r$ and another from the turbulence $(R_{rr} - R_{\phi\phi})/r$. The MMB-$r$ equation (2.6a) can be used to determine the mean pressure distribution in the TCF system. In the present work, we will focus on the properties of the mean momentum balance equation in the azimuthal direction, which is analogous to the streamwise direction in a turbulent pipe or channel flow.

The MMB-ϕ equation (2.6b) represents the balance of three forces in the ϕ direction: a viscous force F_{visc}, a Reynolds shear force $F_{turb\text{-}\phi}$ and a turbulent Coriolis force F_{cori}. In the present work, the MMB-ϕ equation (2.6b) is analysed to reveal the properties of the Reynolds shear stress, the turbulent Coriolis force and the layer structure of a turbulent TCF. A multiscaling analysis of the MMB-ϕ equation (2.6b) is then developed and verified by DNS data.

2.1. *Properties of the Reynolds shear stress*

Multiplying the MMB-ϕ equation (2.6b) by r^2, simple mathematical manipulation gives

$$0 = \frac{\mathrm{d}}{\mathrm{d}r}\left(r^2 \nu\left(\frac{\mathrm{d}U_\phi}{\mathrm{d}r} - \frac{U_\phi}{r}\right)\right) + \frac{\mathrm{d}(r^2 R_{r\phi})}{\mathrm{d}r}. \tag{2.7}$$

Equation (2.7) is equivalent to (9.2.1.) in Townsend (1980), and is also essentially the same as (3.3) in Eckhardt, Grossmann & Lohse (2007).

In a fully developed turbulent TCF, the moment of the viscous shear stress is

$$M_{visc} = 2\pi r L \tau_{r\phi} r = (2\pi L\rho)r^2 \nu\left(\frac{\mathrm{d}U_\phi}{\mathrm{d}r} - \frac{U_\phi}{r}\right), \tag{2.8}$$

and the moment of the Reynolds shear stress is

$$M_{turb} = 2\pi r L \rho R_{r\phi} r = (2\pi L \rho) r^2 R_{r\phi}. \tag{2.9}$$

Hence, equation (2.7) can be presented in the form of moment as

$$0 = \frac{\mathrm{d}M_{visc}}{\mathrm{d}r} + \frac{\mathrm{d}M_{turb}}{\mathrm{d}r}. \tag{2.10}$$

Integrating the mean momentum equation (2.7) or (2.10) in the wall-normal direction from the inner cylinder and applying boundary conditions yields

$$r^2 \nu \left(\frac{\mathrm{d}U_\phi}{\mathrm{d}r} - \frac{U_\phi}{r} \right) + r^2 R_{r\phi} = r^2 \nu \left(\frac{\mathrm{d}U_\phi}{\mathrm{d}r} - \frac{U_\phi}{r} \right) \bigg|_{r=r_i} + (r^2 R_{r\phi}) \big|_{r=ri} = -r_i^2 u_{\tau,i}^2. \tag{2.11}$$

Note that the Reynolds shear stress at the inner cylinder is zero for a turbulent TCF with smooth walls. As mentioned in the previous section, the coordinate system is set up such that the mean azimuthal velocity gradient and the Reynolds shear stress are both negative. Thus, the total moment is also negative. Equation (2.11) is equivalent to (9.2.2) in Townsend (1980), and is also essentially the same as the identity equation (3.4) in Eckhardt *et al.* (2007). Townsend (1980) interpreted equation (2.11) as follows: 'the sum of the 'couples' transmitted by viscous and turbulent stress across surfaces of constant radius is independent of the radius'. Eckhardt *et al.* (2007) called the constant the angular velocity current. Here, a simple interpretation of (2.11) is that the total moment (per $2\pi\rho L$), viscous plus turbulent $M_{visc} + M_{turb}$, is a constant, independent of the radial location. The constancy of (2.11) has been used as a consistency check for DNS simulations, as by Dong (2008).

To establish a turbulent plane Couette flow, one can move the top plate only, or the bottom plate only or move both plates in the same direction or opposite direction. However, the total shear stress, viscous plus turbulent $\tau_{wu} + R_{wu}$, is always a constant across the channel, regardless of how the top and bottom plates are being moved. Similarly, equation (2.11) also indicates that the total moment in a turbulent TCF is always a constant, regardless of Π_Ω or how the inner and outer cylinders are being rotated.

In turbulent channel or boundary layer flows, viscous shear stress peaks at the wall and decreases rapidly away from the wall. In a turbulent TCF, the moment of viscous shear stress also peaks at the wall and decreases rapidly along the wall-normal direction. Away from the wall, the viscous term in the integrated MMB-ϕ (2.11) becomes negligible and the Reynolds shear stress can be approximated as

$$R_{r\phi} \approx -\frac{r_i^2}{r^2} u_{\tau,i}^2. \quad \text{Core Region} \tag{2.12}$$

Hence, Reynolds shear stress in the core of a highly turbulent TCF decreases in a $1/r^2$ fashion along the radial direction.

Following the convention commonly followed for turbulent wall-bounded flows, the Reynolds shear stress normalized by $u_{\tau,i}^2$ is denoted as $R_{r\phi}^+ = R_{r\phi}/u_{\tau,i}^2$. Equation (2.12) in the non-dimensional form can be presented as

$$R_{r\phi}^+ \approx - \left(\frac{r_i}{r} \right)^2 = - \left(\frac{1}{1 + \dfrac{\delta}{r_i} z^-} \right)^2 = - \left(\frac{1 - A_t}{1 - A_t + A_t z^-} \right)^2, \tag{2.13a}$$
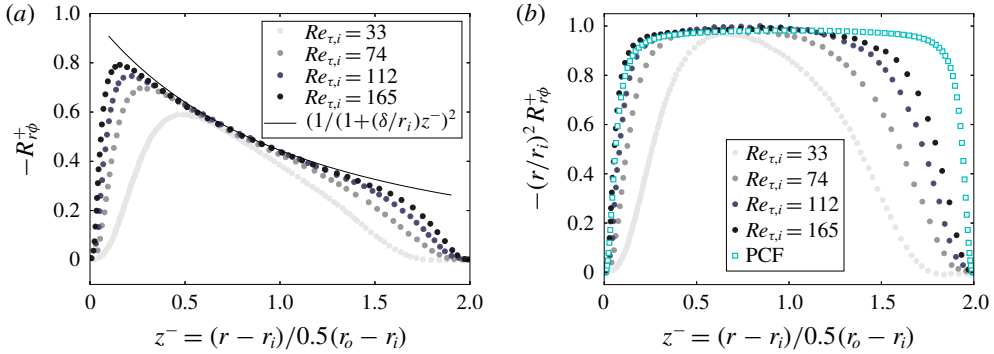
FIGURE 2. (*a*) Reynolds shear stress in a Taylor–Couette flow. The curve is (2.13*a*). Data are from DNS of Dong (2008), with $r_i/r_o = 0.5$ or $A_t = 1/3$. (*b*) $-(r/r_i)^2 R_{r\phi}^+$ versus the wall-normal distance scaled by the TCF gap half-width z^-. The PCF data are from DNS of Kawamura, Abe & Shingai (2000) at $Re_\tau = 181$.

$$\text{or} \quad \left(\frac{r}{r_i}\right)^2 R_{r\phi}^+ \approx -1. \qquad (2.13b)$$

Here, z^- and A_t are defined as

$$z^- \overset{\text{def}}{=} \frac{r - r_i}{0.5(r_o - r_i)} = \frac{r - r_i}{\delta}; \qquad (2.14a)$$

$$A_t \overset{\text{def}}{=} \frac{\delta}{r_{ctr}} = \frac{0.5(r_o - r_i)}{0.5(r_o + r_i)}. \qquad (2.14b)$$

Note that, in studies of pressure- or shear-driven turbulent wall-bounded flows, the wall-normal distance scaled by the channel half-width or the boundary layer height is typically denoted as η (see, e.g. Tennekes & Lumley (1972)). However, η has been used in previous studies of TCF to denote the ratio of the cylinder radii. In the present work, a new notation z^- is introduced to denote the wall-normal distance $r - r_i$ scaled by the TCF gap half-width δ.

The definition of A_t in (2.14*b*) is analogous to the Atwood number used in the study of hydrodynamic instability in density stratified flows, such as Rayleigh–Taylor instability (Glimm *et al.* 2001; Livescu *et al.* 2009; Wei & Livescu 2012), see appendix A. In the present work, therefore, this non-dimensional number is called a geometry Atwood number.

The approximate equation (2.13*a*) for the Reynolds shear stress is compared with DNS data of Dong (2008) in figure 2. The DNS is for the same gap geometry with $A_t = 1/3$, and four different Reynolds numbers. At $Re_{\tau,i} = \delta u_{\tau,i}/\nu = 32.7$, the Reynolds shear stress profile in the core of the gap deviates from (2.13*a*), because at such a low Reynolds number, turbulence is still not well established and the viscous shear stress is not negligible in the outer layer. However, at higher Reynolds numbers, $Re_{\tau,i} > 74$, DNS data of Reynolds shear stress in the core of the gap agree well with (2.13*a*), supporting the validity of the analysis.

In figure 2(*b*), the approximate equation (2.13*b*) is compared with the DNS data of TCF; the Reynolds shear stress in a turbulent PCF is also plotted. The PCF data are from Kawamura's group at $Re_\tau = 181.3$ (Kawamura *et al.* 2000; Shingai, Kawamura & Matsuo 2000; Tsukahara, Kawamura & Shingai 2006). Figure 2(*b*) displays the
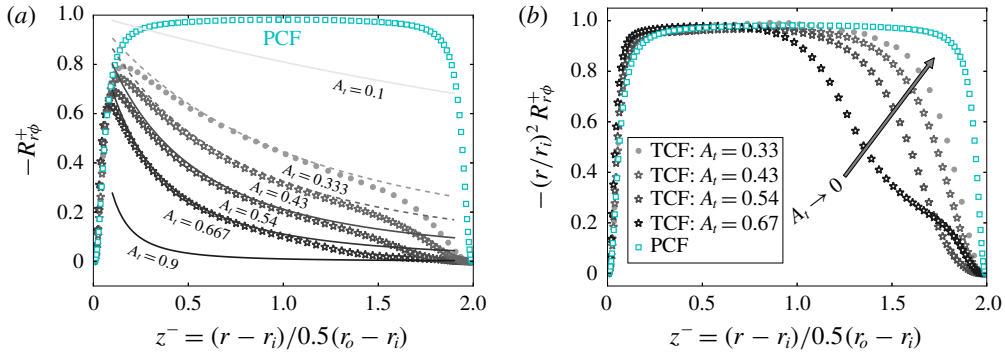
FIGURE 3. Effects of geometry Atwood number A_t on the shape of Reynolds shear stress in TCF. (a) $-R_{r\phi}^+$ versus z^-. The curve is the approximate equation (2.13a). Data for $A_t = 0.333$ are from DNS of Dong (2008). Data for $A_t = 0.43$, 0.54 and 0.667 are from DNS of Tanaka *et al.* (2018). (b) $-(r/r_i)^2 R_{r\phi}^+$ versus z^-. For comparison, Reynolds shear stress of a plane Couette flow is also presented. The data are from DNS of Kawamura's group $Re_\tau = 181.3$ (Kawamura *et al.* 2000; Shingai *et al.* 2000; Tsukahara *et al.* 2006).

resemblance between the turbulent TCF and PCF, and in particular in the inner half next to the inner cylinder. Near the outer cylinder, $-(r/r_i)^2 R_{r\phi}^+$ is different from the Reynolds shear stress in a turbulent plane Couette flow, but the difference becomes smaller as the Reynolds number increases.

In a turbulent plane Couette flow, the Reynolds shear stress is symmetric about the gap centreline, with a peak at the middle. In a turbulent TCF, the mid-gap is located at $r_{ctr} = 0.5(r_i + r_0)$, and its Reynolds shear stress can be approximated as

$$R_{r\phi}|_{ctr} \approx -\left(\frac{r_i}{0.5(r_i + r_o)}\right)^2 u_{\tau,i}^2 = -(1 - A_t)^2 u_{\tau,i}^2. \tag{2.15}$$

Hence, the magnitude of the Reynolds shear stress at the mid-gap of a turbulent TCF is always smaller than $u_{\tau,i}^2$ or $|R_{r\phi}^+| \leqslant 1$. As the geometry Atwood number approaches zero $A_t \to 0$ or the small-gap limit, the Reynolds shear stress at the mid-gap approaches the kinematic wall shear stress at the inner cylinder $|R_{r\phi}|_{ctr} \approx u_{\tau,i}^2$, and the turbulent TCF becomes similar to a turbulent plane Couette flow. However, at a large geometry Atwood number $A_t \to 1$, the magnitude of the Reynolds shear stress is much smaller than $u_{\tau,i}^2$ or $|R_{r\phi}^+| \ll 1$, as shown figure 3(a).

The effect of the geometry Atwood number A_t on the Reynolds shear stress is displayed in figure 3. The approximate equation (2.13a) is compared with DNS data of Tanaka *et al.* (2018) for three geometry Atwood numbers: $A_t = 0.43$, 0.54, 0.667. Also shown are the DNS data of Dong (2008) for $A_t = 0.333$. Curves at $A_t = 0.1$ and $A_t = 0.9$ are plotted to illustrate the trend at low and high geometry Atwood numbers. As A_t approaches zero, the shape of the Reynolds shear stress becomes similar to that of a turbulent plane Couette flow. On the other hand, as A_t approaches 1, Reynolds shear stress is very small, except within a thin layer next to the inner cylinder.

Figure 3(b) shows that $-(r/r_i)^2 R_{r\phi}^+$ in the inner half of a turbulent TCF resembles the shape of the Reynolds shear stress in a turbulent plane Couette flow, even at large geometry Atwood numbers. However, in the outer half, $-(r/r_i)^2 R_{r\phi}^+$ in a turbulent TCF is lower than the Reynolds shear stress in a turbulent plane Couette flow. The difference becomes smaller as the Atwood number decreases.
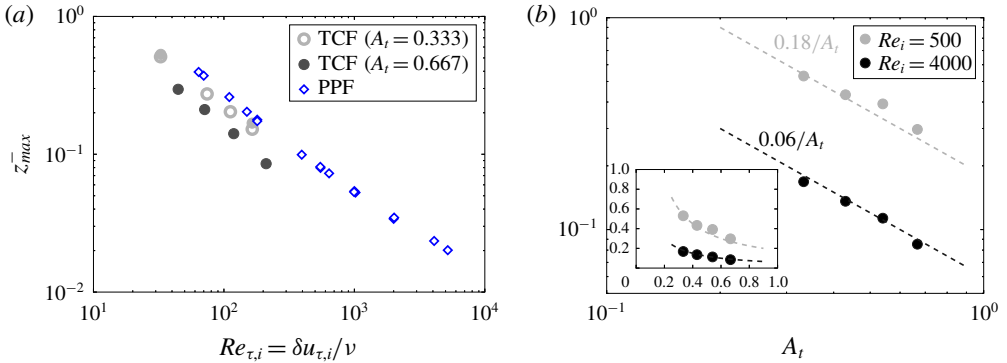
FIGURE 4. Peak Reynolds shear stress location. (*a*) Effect of Reynolds number. Open circles are DNS of TCF by Dong (2008) for $A_t = 0.333$, and filled circles are DNS of TCF by Tanaka *et al.* (2018) for $A_t = 0.333$ and $A_t = 0.668$. DNS data of turbulent plane Poiseuille flow (PPF) are from three independent groups: Kawamura's group (Kawamura *et al.* 2000; Abe, Kawamura & Matsuo 2001), Moser's group (Lee & Moser 2015) and Pirozzoli's group (Pirozzoli, Bernardini & Orlandi 2016). (*b*) Effect of geometry Atwood number. Note that inset is plotted in linear–linear axes. Data are from DNS of Tanaka *et al.* (2018).

In a turbulent TCF, the peak Reynolds shear stress always occurs in the inner half (next to the inner cylinder), as shown in figures 2 and 3. The peak location depends on the Reynolds number and the geometry Atwood number. In figure 4(*a*), the peak Reynolds shear stress location z_{max}^- is plotted versus the Reynolds number. DNS data of TCF for $A_t = 0.333$ are from independent studies by Dong (2008) (open circles in the figure) and Tanaka *et al.* (2018) (filled circles). DNS data at $A_t = 0.667$ are from DNS of Tanaka *et al.* (2018). At the same Reynolds number, the peak Reynolds shear stress location moves closer to the inner cylinder as the geometry Atwood number increases. For the same geometry Atwood number, the peak location moves closer to the inner cylinder as the Reynolds number increases.

In a pressure-driven turbulent channel or pipe flow or a shear-driven turbulent flow over a flat plate, the peak Reynolds shear stress location is a geometric mean of the inner and outer length scales $z_{max} \sim \sqrt{\delta \nu / u_\tau}$ or $z_{max}^- \sim 1/\sqrt{Re_\tau}$ (see Long & Chen 1981; Afzal 1982; Sreenivasan & Sahay 1997; Wei *et al.* 2005). For comparison, therefore, DNS data for a pressure-driven channel flow are also plotted in figure 4(*a*). The presently available TCF data seem to follow a trend similar to those in a pressure-driven turbulent channel flow. In other words, the peak Reynolds shear stress location in a turbulent TCF also occurs at the meso length scale $\sqrt{\delta \nu / u_{\tau,i}}$. However, the Reynolds numbers of the TCF data used in the present work are low to moderate, and the trend at high Reynolds numbers remains to be investigated.

The effect of the geometry Atwood number A_t on the peak location of the Reynolds shear stress is shown in figure 4(*b*). The DNS data are from Tanaka *et al.* (2018) for four geometry Atwood numbers $A_t = 0.333, 0.43, 0.54, 0.667$. The data are for two Reynolds numbers $Re_i = 2\delta r_i \Omega_i / \nu = 500$ and 4000. The corresponding friction Reynolds numbers are listed in table 1. Data for z_{max}^- at $Re_i = 4000$ are smaller than those at $Re_i = 500$, showing the effect of Reynolds number as presented in figure 4(*a*).

As shown in figure 3(*a*), the peak Reynolds shear stress location z_{max}^- becomes smaller with increasing A_t, meaning that the peak Reynolds shear stress location moves closer to the inner cylinder. (In a turbulent TCF, the peak Reynolds shear stress

$Re_i = \dfrac{2\delta r_i \Omega_i}{\nu} = 500$	A_t		0.333	0.43	0.54	0.667
	Π_Ω		-2	-2.5	-3.33	-5
	$Re_{\tau,i} = \dfrac{\delta u_{\tau,i}}{\nu}$		44.6	37.9	35.0	32.8
$Re_i = \dfrac{2\delta r_i \Omega_i}{\nu} = 4000$	A_t		0.333	0.43	0.54	0.667
	Π_Ω		-2	-2.5	-3.33	-5
	$Re_{\tau,i} = \dfrac{\delta u_{\tau,i}}{\nu}$		210.6	188.2	174.9	164.6

TABLE 1. Parameters of DNS by Tanaka *et al.* (2018), shown in figure 4(*b*).

will never occur in the outer half of the gap, regardless of the Reynolds number, A_t, or rotation ratio.) The presently available DNS data are limited to moderate geometry Atwood numbers, so the functional dependence at $A_t \to 0$ or $A_t \to 1$ is not clear at this time. Based on the DNS data at moderate A_t, however, geometry Atwood number dependencies can be approximated by a simple power law of $z_{max}^- \sim f(Re)/A_t$. The peak Reynolds shear stress location z_{max}^- is bounded between 0 and 1, and the inset of figure 4(*b*) indicates that this power law cannot be extrapolated to the $A_t \to 0$ limit. An asymptotic analysis might uncover the functional dependence at the small and large Atwood number limits.

Next, the MMB-ϕ equation will be rearranged and integrated to reveal properties of the turbulent Coriolis force.

2.2. *Property of the turbulent Coriolis force*

In previous studies of turbulent TCF, the properties of the turbulent Coriolis force have not been clear. Here, properties of the turbulent Coriolis force are revealed directly from the mean momentum balance equation.

The viscous force in the MMB-ϕ (2.6*b*) is written as a function of the mean azimuthal velocity, but it can be written in more than one form, as shown in appendix B. For example, the MMB-ϕ equation can also be written as

$$0 = \nu \frac{d}{dr}\left(\frac{1}{r}\frac{d(rU_\phi)}{dr}\right) + \frac{dR_{r\phi}}{dr} + \frac{2R_{r\phi}}{r}. \tag{2.16}$$

Integrating the MMB-ϕ (2.16) along the radial direction from the inner cylinder to the outer cylinder yields

$$\int_{r_i}^{r_o} \frac{2R_{r\phi}}{r}\,dr = \left\{\nu \frac{1}{r}\frac{d(rU_\phi)}{dr}\right\}\Bigg|_{r_i} - \left\{\nu \frac{1}{r}\frac{d(rU_\phi)}{dr}\right\}\Bigg|_{r_o} + R_{r\phi}|_{r_i} - R_{r\phi}|_{r_o}. \tag{2.17}$$

For a turbulent TCF with smooth walls, the Reynolds shear stress $R_{r\phi}$ is zero at both the inner and outer cylinders: $R_{r\phi}|_{r_i} = 0$ and $R_{r\phi}|_{r_o} = 0$. The first two terms on the right side of (2.17) can be arranged as

$$\left\{\nu \frac{1}{r}\frac{d(rU_\phi)}{dr}\right\}\Bigg|_{r_i} = \nu\left\{\frac{dU_\phi}{dr} + \frac{U_\phi}{r}\right\}\Bigg|_{r=r_i} = \nu\left\{\frac{dU_\phi}{dr} - \frac{U_\phi}{r} + 2\frac{U_\phi}{r}\right\}\Bigg|_{r=r_i}, \tag{2.18a}$$

$$\left\{\nu \frac{1}{r}\frac{d(rU_\phi)}{dr}\right\}\Bigg|_{r_o} = \nu\left\{\frac{dU_\phi}{dr} + \frac{U_\phi}{r}\right\}\Bigg|_{r=r_o} = \nu\left\{\frac{dU_\phi}{dr} - \frac{U_\phi}{r} + 2\frac{U_\phi}{r}\right\}\Bigg|_{r=r_o}. \tag{2.18b}$$
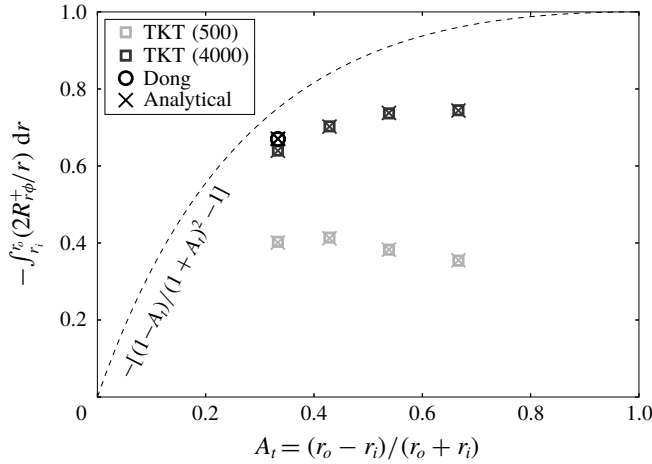
FIGURE 5. Verification of the global integral equation (2.20) for the turbulent Coriolis force against DNS data. Parameters for the DNS data of Tanaka *et al.* (2018) are listed in table 1, and the TCF is counter-rotating with $\Pi_\Omega = -1/\Pi_r = -(1+A_t)/(1-A_t)$. TKT (500) refers to the data of Tanaka *et al.* at $Re_i = 500$, and TKT (4000) at $Re_i = 4000$. DNS of Dong (2007) was for fixed outer cylinder or $\Pi_\Omega = \infty$, $Re_i = 8000$, $Re_{\tau,i} = 225$ and $A_t = 0.333$. The cross symbols are the right side of (2.20). The dashed curve is the first part on the right side of (2.20).

Note that $(U_\phi/r)_{r=r_i} = \Omega_i$ and $(U_\phi/r)_{r=r_o} = \Omega_o$. As mentioned in the previous section, the coordinate system is set up such that the mean azimuthal velocity decreases in the radial direction, or dU_ϕ/dr is negative. Thus, the definition of friction velocities in (2.3a) and (2.3b) leads to $\nu(dU_\phi/dr - U_\phi/r)_{r=r_i} = -u_{\tau,i}^2$ and $\nu(dU_\phi/dr - U_\phi/r)_{r=r_o} = -u_{\tau,o}^2$.

Substituting the boundary condition (2.18a) and (2.18b) and the boundary conditions for $R_{r\phi}$, the global integral equation (2.17) of the turbulent Coriolis force can be written as

$$\int_{r_i}^{r_o} \frac{2R_{r\phi}}{r}\, dr = \{u_{\tau,o}^2 - u_{\tau,i}^2\} - \{2\nu\Omega_o - 2\nu\Omega_i\}. \tag{2.19}$$

Thus, the global integral of the turbulent Coriolis force depends on the wall shear stresses at the inner and outer cylinders, as well as the rotation speeds of the inner and outer cylinders.

Normalizing equation (2.19) by $u_{\tau,i}^2$, the global integral of the turbulent Coriolis force can be expressed as

$$\int_{r_i}^{r_o} \frac{2R_{r\phi}^+}{r}\, dr = \left[\left(\frac{1-A_t}{1+A_t}\right)^2 - 1\right] - \left(\frac{1+A_t}{1-A_t} - 1\right)\left(\frac{1}{\Pi_\Omega} - 1\right)\frac{U_{\phi,i}^+}{Re_{\tau,i}}, \tag{2.20}$$

where $U_{\phi,i}^+ = U_{\phi,i}/u_{\tau,i}$ is the inner cylinder's azimuthal velocity normalized by the friction velocity at the inner cylinder. Equation (2.20) indicates that the global integral of the turbulent Coriolis force depends on the gap geometry A_t, rotation ratio Π_Ω, Reynolds number $Re_{\tau,i}$ and $U_{\phi,i}^+$.

The global integral equation (2.20) for the turbulent Coriolis force is verified by DNS data in figure 5. As shown in figure 5, the integrated $\int_{r_i}^{r_o}(2R_{r\phi}^+/r)\, dr$ (open square or circle) agrees well with the analytical solution (X in the figure). Note that the

$$\int_{r_i}^{r_o} \frac{2R_{r\phi}^+}{r} \, \mathrm{d}r$$

$A_t = 0$	0
$A_t \to 1$	$-1 - \left(\dfrac{1+A_t}{1-A_t} - 1 \right) \left(\dfrac{1}{\Pi_\Omega} - 1 \right) \dfrac{U_{\phi,i}^+}{Re_{\tau,i}}$
$\Pi_\Omega = 0$	$\left[\left(\dfrac{1-A_t}{1+A_t} \right)^2 - 1 \right]$
$\Pi_\Omega = \infty$	$\left[\left(\dfrac{1-A_t}{1+A_t} \right)^2 - 1 \right] + \left(\dfrac{1+A_t}{1-A_t} - 1 \right) \dfrac{U_{\phi,i}^+}{Re_{\tau,i}}$

TABLE 2. The global integral of the turbulent Coriolis force for limiting cases.

turbulent Coriolis force is negative in the coordinate system, and a negative sign is multiplied to both sides of (2.20) in figure 5.

In general, $U_{\phi,i}^+/Re_{\tau,i}$ becomes smaller as the Reynolds number increases. Thus, at high Reynolds numbers, the last part on the right side of (2.20) becomes less important, and the global integral can be approximated by the first part only, represented by the dashed curve in figure 5. The DNS data of Tanaka *et al.* (2018) at $Re_i = 500$ deviate from the dashed curve as shown in figure 5, meaning that rotation ratio is important in the global integral of the turbulent Coriolis force. At a higher Reynolds number of $Re_i = 4000$, the DNS data of Tanaka *et al.* (2018) move closer to the dashed curve, especially for small Atwood numbers.

Using (2.20), the global integral of the turbulent Coriolis force under four limiting cases is determined and listed in table 2. For the limiting case of a small gap ($r_i \approx r_o$ or $A_t \to 0$), the global integral of the turbulent Coriolis force approaches zero, meaning that the Coriolis force is not important for a small-gap TCF. In other words, in the limit of $A_t \to 0$, a turbulent TCF becomes a turbulent plane Couette flow. On the other hand, for a turbulent TCF with a large gap or $A_t \to 1$, the effect of rotation ratio can become significant because $(1+A_t)/(1-A_t)$ approaches infinity. At the large-gap limit ($A_t = 1$), the global integral of the turbulent Coriolis force $\int_{r_i}^{r_o} (2R_{r\phi}^+/r) \, \mathrm{d}r$ approaches -1 or $\int_{r_i}^{r_o} (2R_{r\phi}/r) \, \mathrm{d}r$ approaches $-u_{\tau,i}^2$.

For the case of only the outer cylinder rotating ($\Pi_\Omega = 0$), the last part in (2.20) is zero because the azimuthal velocity of the inner cylinder is zero or $U_{\phi,i}^+ = 0$. For the case of inner cylinder rotating only ($\Pi_\Omega = \infty$), the term $(1/\Pi_\Omega - 1)$ in (2.20) becomes -1.

3. Scaling analysis of the MMB-ϕ equation

The variables in the MMB equation (2.6b) can be scaled in a number of ways (Fife *et al.* 2005; Fife 2006). All versions are mathematically equivalent, but only some of them reflect naturally the behaviour of the actual functions U_ϕ and $R_{r\phi}$. In this section, a general form of normalization is first presented, then the general form will be used to develop an inner scaling and an outer scaling.

To be general, the length in the spatial derivation dr and the radial location r are scaled by different length scales

$$dr^* \stackrel{\text{def}}{=} \frac{dr}{l_{ref}}; \quad r^* \stackrel{\text{def}}{=} \frac{r}{r_{ref}}. \tag{3.1a,b}$$

A superscript asterisk denotes a normalized variable; l_{ref} is a reference length for the spatial variation in the radial direction dr, and r_{ref} is a reference scale for the radial location that is involved in the turbulent Coriolis force.

In previous studies of TCF, the length in the spatial derivative dr in the velocity gradient and the radial location r in the turbulent Coriolis force have often been normalized by the same reference length scale, commonly the gap width 2δ. For the velocity gradient dU_ϕ/dr or the Reynolds shear stress gradient $dR_{r\phi}/dr$, the velocity or the Reynolds shear stress varies spatially between r_i and r_o. Hence, it is reasonable to use the gap width 2δ or half-width δ as a reference length scale for the wall-normal distance. For example, the wall-normal location normalized by δ will vary between 0 and 1 from the inner cylinder to the mid-gap. In contrast, the radial location r in the turbulent Coriolis force varies from r_i to r_o. Normalized by δ, the radial location r in the turbulent Coriolis force varies between r_i/δ and r_o/δ. For a TCF with a small gap $r_i \gg \delta$, then $r_i/\delta \gg 1$ and $r_o/\delta \gg 1$. For a TCF with a large gap $\delta \gg r_i$, then $r_i/\delta \ll 1$ and $r_o/\delta \sim o(1)$.

The mean azimuthal velocity and Reynolds shear stress are normalized as

$$U_\phi^* \stackrel{\text{def}}{=} \frac{U_\phi}{U_{\phi,ref}}; \quad R_{r\phi}^* \stackrel{\text{def}}{=} \frac{R_{r\phi}}{R_{r\phi,ref}}, \tag{3.2a,b}$$

where $U_{\phi,ref}$ is a reference velocity scale, and $R_{r\phi,ref}$ is a reference scale for the Reynolds shear stress.

Substituting the normalized variables in (3.1) and (3.2) into the MMB-ϕ (2.6b), a general form of the non-dimensional MMB-ϕ equation can be expressed as

$$0 = \left[\frac{\nu}{l_{ref} U_{\phi,ref}} \frac{U_{\phi,ref}^2}{R_{r\phi,ref}} \right] \frac{d}{dr^*} \left(\frac{1}{r^*} \frac{d}{dr^*} (r^* U_\phi^*) \right) + \frac{dR_{r\phi}^*}{dr^*} + \left[\frac{l_{ref}}{r_{ref}} \right] \frac{2R_{r\phi}^*}{r^*}. \tag{3.3}$$

Pressure-driven turbulent wall-bounded flows, such as pipe or channel flow, or shear-driven turbulent flow over a flat plate can be divided into several layers. (This concept can be dated back to Prandtl in 1904, see, for example, Tennekes & Lumley (1972).) The characteristic length scale and velocity scale are different in different layers of the flow. Proper scaling of the flow and the equation require determining appropriate length and velocity scales for the different layers. Next, therefore, a new three-layer structure is proposed for a turbulent TCF and proper length and velocity scales are determined for the inner and outer layers. Equation (3.3) will be used to present an inner and an outer scaling of the MMB-ϕ equation.

3.1. *Layer structure of a turbulent TCF*

One way to describe the layered structure of a turbulent flow is through the characteristic of the force balance in the mean momentum balance equation. This approach has been used to reveal the layer structure in pressure- or shear-driven turbulent wall-bounded flows (Wei *et al.* 2005; Klewicki *et al.* 2007). A similar
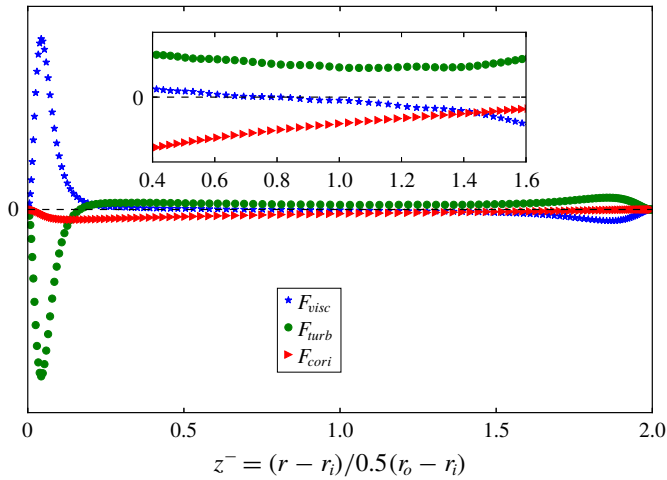
FIGURE 6. Three forces in the MMB-ϕ (2.6b). The data are from the DNS of Tanaka *et al.* (2018). The case is a counter-rotating TCF with $r_i/r_0 = 0.5$ or $A_t = 1/3$. The Reynolds number of the simulation is $(2\delta r_i|\Omega_i|)/\nu = (2\delta r_o|\Omega_o|)/\nu = 4000$. The corresponding friction Reynolds numbers are $Re_{\tau,i} = \delta u_{\tau,i}/\nu \approx 165$ and $Re_{\tau,o} = \delta u_{\tau,o}/\nu \approx 82$. The magnitudes of the forces are not shown in the figure, for they depend on the method of normalization.

approach has been applied to uncover the layer structure of passive scalar transport in a turbulent channel flow (Wei 2018) and buoyancy-driven turbulent flow and heat transfer in a differentially heated vertical channel (Wei 2019).

For a turbulent TCF, the typical shapes of the three forces in the MMB-ϕ (2.6b) are illustrated in figure 6. The magnitudes of the forces are not shown in the figure, for they depend on the method of normalization, but the shapes and relative magnitudes do not depend on the normalization. Adjacent to the inner cylinder, the viscous force is positive, or a driving force, and the turbulent force is negative, or a drag force. The directions of the forces are reversed adjacent to the outer cylinder, where the turbulent force is a driving force and the viscous force is a drag force.

Starting from zero at the inner cylinder wall, the viscous force rises sharply to a peak value, then decreases sharply away from the wall. In the meantime, the Reynolds shear force starts from zero at the inner cylinder and decreases sharply to a minimum, then rises sharply away from the inner cylinder. Adjacent to the inner cylinder the force balance is between the viscous force and the Reynolds shear force. In the core of the gap, the viscous force is essentially zero and the Reynolds shear force is positive, but the magnitude is much smaller than that adjacent to the inner cylinder. Approaching the outer cylinder, the force balance is again balanced by the viscous force and Reynolds shear force. Thus, the force balance in the MMB-ϕ (2.6b) undergoes a series of transitions at the intersections of the different layers.

One way to assess the contributions of different forces to the balance of the MMB-ϕ (2.6b) is by plotting the ratio of two forces (Wei *et al.* 2005; Klewicki *et al.* 2007; Wei 2018, 2019). The ratio between the viscous force and the turbulent force F_{visc}/F_{turb} in a TCF is shown in figure 7(a). For comparison, the force ratio F_{visc}/F_{turb} in a pressure-driven turbulent channel flow is shown figure 7(b).

In a pressure-driven turbulent channel flow, the Reynolds shear force is zero near the channel wall, where the force balance is between the pressure force and the viscous
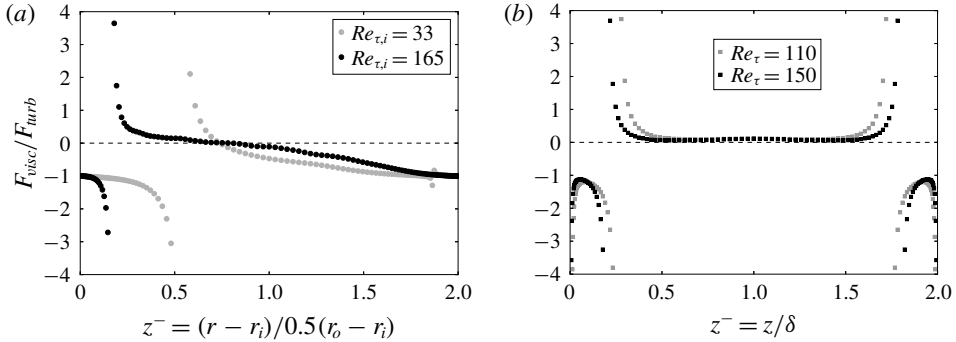
FIGURE 7. (*a*) Ratio between the viscous force and Reynolds shear force F_{visc}/F_{turb} in the MMB-ϕ (2.6*b*) for a TCF. Data are from DNS of Tanaka *et al.* (2018) for $r_i/r_o = 0.5$ ($A_t = 0.33$) and $(r_o - r_i)r_i|\Omega_i|/\nu = 500$ and 4000. (*b*) Ratio of F_{visc}/F_{turb} in a pressure-driven plane channel flow. Here z is the wall-normal distance, and δ is the channel half-width. Data are from DNS by Kawamura's group (Kawamura *et al.* 2000; Shingai *et al.* 2000; Tsukahara *et al.* 2006).

force. Thus, the force ratio F_{visc}/F_{turb} in a turbulent channel flow starts from a large negative value at the channel wall. In a turbulent TCF, the turbulent Coriolis force is zero near the inner cylinder, where the force balance is between the viscous force and Reynolds shear force. Thus, the force ratio F_{visc}/F_{turb} in a turbulent TCF is -1 at the inner cylinder. At sufficiently high Reynolds numbers, the inner half of a TCF exhibits a structure similar to that in the lower or upper half of a turbulent channel flow. The flow structure in a turbulent channel flow is symmetric about the channel centreline, but the flow structure in a TCF is not symmetric, because the friction velocity at the inner cylinder is different from that at the outer cylinder.

Based on the characteristics of the force ratio presented in figure 7, the inner half of a turbulent TCF can be divided into at least three layers:

(i) Layer I, an inner layer where the force balance is between the viscous force and the Reynolds shear force: $|F_{visc}| \approx |F_{turb}|$.

(ii) Layer II, a meso layer centred around the peak Reynolds shear stress location.

(iii) Layer III, an outer layer where the viscous force is negligible and the force balance is between the Reynolds shear force and the turbulent Coriolis force: $|F_{cori}| \approx |F_{turb}|$.

The three-layer structure for the inner half of a turbulent TCF is sketched in figure 8.

We note that the DNS data used in this work are limited to relatively moderate Reynolds number. In particular, the friction Reynolds number for the outer half of a TCF, $Re_{\tau,o} = \delta u_{\tau,o}/\nu$, is small. Thus, for the two cases shown in figure 7(*a*) the friction Reynolds numbers for the outer half are $Re_{\tau,o} = 16.5$, and 82.5. In the DNS of Tanaka *et al.* (2018), the lowest Reynolds number case, $Re_{\tau,i} = 33$ and $Re_{\tau,o} = 16.5$, has not achieved a fully developed turbulent state yet, and the flow in the outer half is more laminar like. For their highest Reynolds number case of $Re_{\tau,i} = 165$ and $Re_{\tau,o} = 82.5$, the inner half displays a well-established three-layer structure, but the layer structure of the outer half is very different.

The thickness of Layers I, II and III will depend on the Reynolds number, the geometry Atwood number and likely the rotation ratio Π_Ω. More DNS data
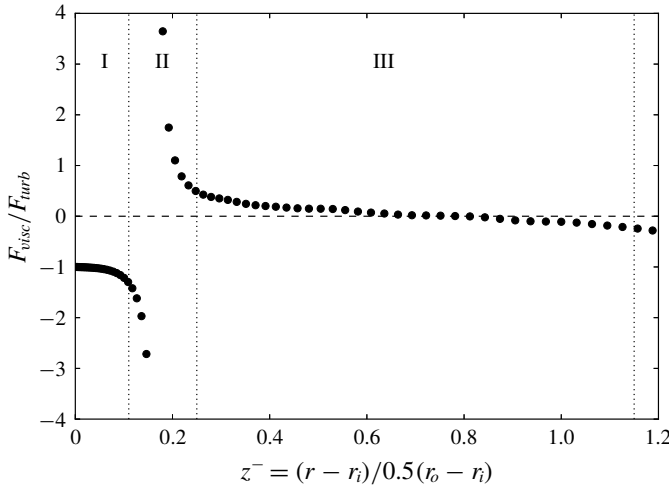
FIGURE 8. Sketch of the layer structure in the inner half of a turbulent TCF. The data points are from DNS of Tanaka *et al.* (2018) for $Re_i = 4000$ and $A_t = 0.333$ ($Re_{\tau,i} = 164.6$).

are required to determine the thickness and the dependencies on the controlling non-dimensional numbers.

3.2. *Scaling for Layer* III *of the inner half*

In the outer Layer III shown in figure 8, a natural length scale for the spatial variation in the radial direction dr is the gap half-width, $l_{ref} = \delta$. A reasonable length scale for the radial location is the mid-gap location $r_{ref} = r_{ctr} = 0.5(r_i + r_o)$. The friction velocity $u_{\tau,i}$ is used as a reference velocity scale $U_{\phi,ref} = u_{\tau,i}$, as in pressure- or shear-driven turbulent wall-bounded flows. The Reynolds shear stress at the TCF mid-gap is used as a reference scale for the Reynolds shear stress $R_{r\phi,ref} = |R_{r\phi}|_{ctr}$. The scaled variables for Layer III are denoted as follows

$$z^- \stackrel{\text{def}}{=} \frac{r - r_i}{\delta}; \quad \mathrm{d}z^- \stackrel{\text{def}}{=} \frac{\mathrm{d}r}{\delta}; \quad r^* \stackrel{\text{def}}{=} \frac{r}{r_{ctr}}; \quad U_\phi^+ \stackrel{\text{def}}{=} \frac{U_\phi}{u_{\tau,i}}; \quad R_{r\phi}^* \stackrel{\text{def}}{=} \frac{R_{r\phi}}{|R_{r\phi}|_{ctr}}. \qquad (3.4a\text{–}e)$$

Substituting the outer-scaled variables into (3.3), the outer-scaled MMB-ϕ equation can be presented as

$$0 = \left[\frac{u_{\tau,i}^2}{|R_{r\phi}|_{ctr}} \frac{1}{Re_{\tau,i}}\right] \frac{\mathrm{d}}{\mathrm{d}z^-}\left(\frac{1}{r^*}\frac{\mathrm{d}}{\mathrm{d}z^-}(r^* U_\phi^+)\right) + \frac{\mathrm{d}R_{r\phi}^*}{\mathrm{d}z^-} + A_t\frac{2R_{r\phi}^*}{r^*}. \qquad (3.5)$$

For a small gap with $r_i \approx r_o$ or $A_t \approx 0$, $|R_{r\phi}|_{ctr} \approx u_{\tau,i}^2$ as shown above. Hence, a proper outer scaling for a turbulent TCF at small geometry Atwood number is

$$0 = \left[\frac{1}{Re_{\tau,i}}\right] \frac{\mathrm{d}}{\mathrm{d}z^-}\left(\frac{1}{r^*}\frac{\mathrm{d}}{\mathrm{d}z^-}(r^* U_\phi^+)\right) + \frac{\mathrm{d}R_{r\phi}^+}{\mathrm{d}z^-} + A_t\frac{2R_{r\phi}^+}{r^*}. \qquad (3.6)$$

This outer-scaled MMB-ϕ equation involves two non-dimensional numbers: A_t and a friction Reynolds number $Re_{\tau,i} = \delta u_{\tau,i}/\nu$. An advantage of using $u_{\tau,i}^2$ instead of
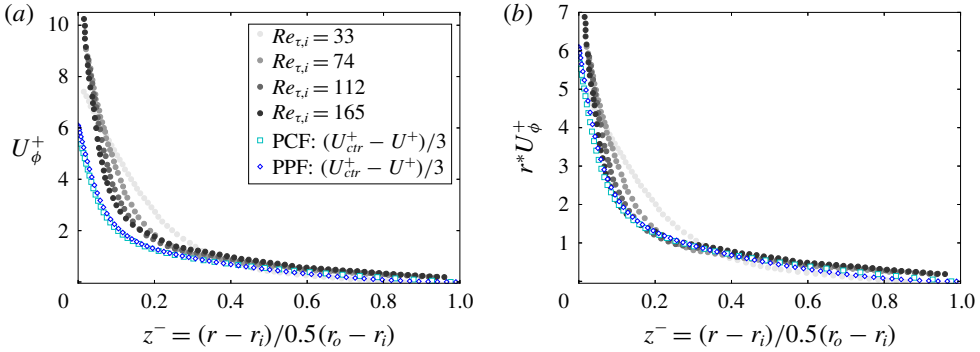
FIGURE 9. Mean azimuthal velocity in outer scaling. Data are from DNS of Dong (2008) with $A_t = 1/3$. (a) U_ϕ^+ versus z^-. (b) $r^* U_\phi^+$ versus z^-. PCF data are from DNS of Kawamura *et al.* (2000) at $Re_\tau = 181$. PPF data are from Moser, Kim & Mansour (1999) at $Re_\tau = 180$.

$|R_{r\phi}|_{ctr}$, from a practical perspective, is that $u_{\tau,i}$ can be directly obtained from the measurement of the mean torque at either the inner cylinder or the outer cylinder. Based on dimensional analysis, $|R_{r\phi}|_{ctr}$ is a function of A_t and $Re_{\tau,i}$ and Π_Ω. Therefore, for simplicity, $u_{\tau,i}^2$ will be used as a reference scale for the Reynolds shear stress, even when $|R_{r\phi}|_{ctr}$ is much smaller than $u_{\tau,i}^2$, when A_t is not small.

Figure 9 presents the DNS data of the mean azimuthal velocity for the same A_t and Π_Ω, but different Reynolds numbers. In figure 9(a), the DNS data are presented as the inner-scaled mean azimuthal velocity U_ϕ^+ versus the outer-scaled wall-normal distance z^-. In figure 9(b), the DNS data are presented as the normalized angular momentum $r^* U_\phi^+$ versus the outer-scaled wall-normal distance z^-. Figure 9 shows that the data at $Re_{\tau,i} = 33$ deviate from the higher Reynolds number data. This deviation is the low Reynolds number effect, as in canonical turbulent channel or pipe flows (Tennekes & Lumley 1972).

In a turbulent plane Couette flow or a turbulent plane Poiseuille flow, the coordinate system is typically set up so the mean velocity at the wall is 0 and the scaling of the mean velocity for the outer layer is usually the so-called mean velocity deficit: $U_{ctr} - U$. In a TCF, the mean azimuthal velocity at the inner cylinder is usually set as $U_{\phi,i} = r_i \Omega_i$. Hence, the profile of U_ϕ in a TCF is analogous to the mean velocity deficit in a plane Couette flow. For comparison, the mean velocity deficit $U_{ctr}^+ - U^+$ for a pressure-driven turbulent channel flow and a turbulent plane Couette flow are also presented in figure 9.

In figure 9, the mean velocity deficits for PCF and PPF are multiplied by an empirical factor of 1/3, to demonstrate the similar trend between TCF and PCF or PPF. The multiplying factor is related to the pre-factor in the viscous force term in (3.5): $u_{\tau,i}^2/|R_{r\phi}|_{ctr} \approx 1/(1 - A_t)^2 \geqslant 1$. Compared with PCF or PPF, the core region of a turbulent TCF is better mixed and the mean velocity gradient is smaller. For a small Atwood number $A_t \to 0$, the mean azimuthal velocity in a turbulent TCF will approach the mean velocity deficit in a turbulent plane Couette flow.

In a pressure-driven turbulent channel flow, the mean velocity is symmetric about the channel centreline. In a shear-driven turbulent plane Couette flow, on the other hand, the mean velocity is anti-symmetric about the channel centreline. In either case, the mean velocity deficit will be exactly zero at the channel centreline $z^- = 1$. Notably,

in a turbulent TCF, the mean flow is not anti-symmetric about the mid-gap. As shown in figure 9, U_ϕ in general is not zero at $z^- = 1$.

In pressure- or shear-driven turbulent wall-bounded flows, the Reynolds shear stress profiles from different Reynolds numbers collapse well (see Pope 2001), and as shown in figure 2, $R_{r\phi}^+$ from different Reynolds numbers also collapse reasonably well versus z^- for a turbulent TCF. The outer layer scaling for a turbulent TCF and pressure- or shear-driven turbulent wall-bounded flows are similar.

3.3. *Scaling for Layer I of the inner half*

In Layer I of the inner half shown in figure 8, the force balance is between the viscous force and the Reynolds shear force, similar to the inner layer in a pressure-driven turbulent channel or pipe flow. The mean azimuthal velocity will be scaled by $u_{\tau,i}$, and the Reynolds shear stress will also be scaled by $u_{\tau,i}^2$. The distance from the wall $z = r - r_i$ will be scaled by the viscous length scale $\nu/u_{\tau,i}$. The inner scaled variables are denoted as

$$z = r - r_i; \quad \mathrm{d}z^+ \overset{\text{def}}{=} \frac{\mathrm{d}r}{\nu/u_{\tau,i}}; \quad U_\phi^+ \overset{\text{def}}{=} \frac{U_\phi}{u_{\tau,i}}; \quad R_{r\phi}^+ \overset{\text{def}}{=} \frac{R_{r\phi}}{u_{\tau,i}^2}; \quad r^* \overset{\text{def}}{=} \frac{r}{r_{ctr}}. \qquad (3.7a\text{--}e)$$

Substituting the inner-scaled variables into (3.3), the inner-scaled MMB-ϕ equation can be expressed as

$$0 = \frac{\mathrm{d}}{\mathrm{d}z^+} \left(\frac{1}{r^*} \frac{\mathrm{d}}{\mathrm{d}z^+} (r^* U_\phi^+) \right) + \frac{\mathrm{d}R_{r\phi}^+}{\mathrm{d}z^+} + \frac{A_t}{Re_{\tau,i}} \frac{2R_{r\phi}^+}{r^*}. \qquad (3.8)$$

The inner-scaled mean azimuthal velocity profiles are presented in figure 10(*a*). The data are presented as the difference between the mean azimuthal velocity and the inner cylinder velocity (the data are from the DNS of Dong (2008) for four Reynolds numbers). For comparison, the mean streamwise velocity in a turbulent plane Poiseuille flow and a turbulent plane Couette flow are also presented. As Reynolds number increases, the mean velocity U^+ in PPF or PCF exhibits a layer with a logarithmic-like growth. The so-called log layer extends outwards as the Reynolds number increases. The mean relative velocity $U_{\phi,i}^+ - U_\phi^+$ in a turbulent TCF also exhibits a logarithmic-like growth away from the inner cylinder, but the additive constant in the logarithmic function varies with the Reynolds number, as shown in figure 10(*a*).

In figure 10(*b*), the relative angular momentum is plotted as the form in (3.8). DNS data from different Reynolds numbers but the same A_t are seen to collapse reasonably well in the inner region. The relative angular momentum $r^*(U_{\phi,i}^+ - U_\phi^+)$, for $A_t = 1/3$, is below the mean velocity profile in a turbulent PPF or PCF. At the small-gap limit or $A_t \to 0$, the relative angular momentum $r^*(U_{\phi,i}^+ - U_\phi^+)$ in a turbulent TCF will approach the mean velocity distribution of a turbulent channel or Couette flow. On the other hand, for the large-gap limit, the relative angular momentum will become even smaller, as indicated by the arrow for A_t. For a fixed A_t, the relative angular momentum also exhibits a layer with a logarithmic-like growth, and this log layer extends outwards as the Reynolds number increases, indicated by the arrow for *Re*. More DNS simulations are required to study the effect of Atwood number, Reynolds number and rotation ratio.
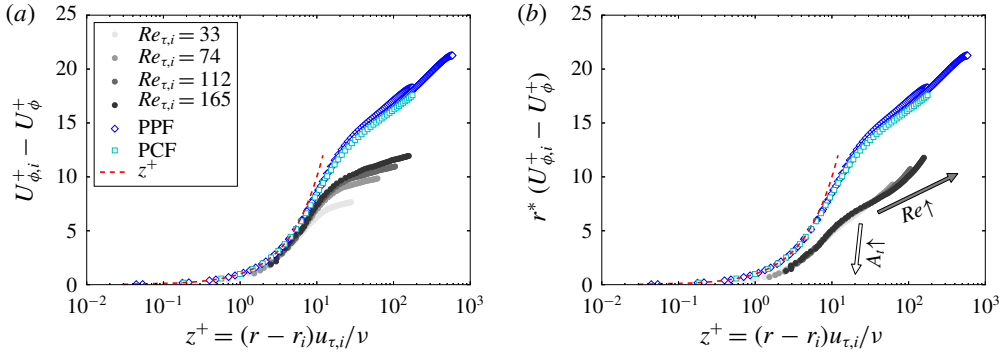
FIGURE 10. Scaling of the mean azimuthal velocity for Layer I of inner half. (*a*) Inner-scaled mean azimuthal velocity relative to the inner cylinder velocity versus the inner-scaled wall-normal distance z^+. (*b*) Inner-scaled mean angular momentum versus z^+. Data are from DNS of Dong (2008) for $A_t = 1/3$. For comparison, DNS data of turbulent plane Couette flow at $Re_\tau = 181$ by Kawamura *et al.* (2000), and DNS data of turbulent channel flow at two Reynolds numbers $Re_\tau = 180$ and 590 by Moser *et al.* (1999) are also plotted.

Note that the boundary condition at the inner cylinder wall can be presented as

$$\left| \left. \frac{\mathrm{d}U_\phi^+}{\mathrm{d}z^+} \right|_{r=r_i} - \frac{U_\phi^+|_{r=r_i}}{\left(\dfrac{1}{A_t} - 1 \right) Re_{\tau,i}} \right| = 1. \tag{3.9}$$

If $U_\phi^+|_{r=r_i} = 0$ (inner cylinder fixed, outer cylinder rotating), the inner-scaled mean azimuthal velocity gradient is 1, similar to that in a turbulent channel or Couette flow. However, if the inner cylinder is not fixed, the inner-scaled mean azimuthal velocity gradient at the wall will be smaller than 1. The difference is minor for small Atwood numbers and/or high Reynolds numbers. This explains why the TCF data in figure 10(*a*) are slightly below the curve of $U^+ = z^+$ (dashed curve in the figure).

DNS data for the inner scaling of the Reynolds shear stress are presented in figure 11. For the same A_t and rotation ratio, the inner-scaled Reynolds shear stress profiles from different Reynolds numbers collapse reasonable well in the inner layer. For comparison, the Reynolds shear stress for a turbulent channel flow at $Re_\tau = 180$ is shown in figure 11(*a*). The inner-scaled Reynolds shear stress in a turbulent TCF displays a trend in Layer I that is similar to the Layer I of a pressure-driven turbulent channel flow.

In figure 11(*b*), the DNS data of $-(r/r_i)^2 R_{r\phi}^+$ in a TCF are plotted, along with the Reynolds shear stress for a turbulent plane Couette flow at $Re_\tau = 181$. The inner-scaled Reynolds shear stress data for TCF at different Reynolds numbers collapse reasonably well. The deviation at $Re_{\tau,i} = 33$ is caused by the low Reynolds number effect.

4. Discussion

In a plane Couette flow, there is only one controlling non-dimensional number: Re_τ. In contrast, there are four controlling parameters in a turbulent TCF: Γ, Π_Ω, A_t and $Re_{\tau,i}$. For sufficiently long cylinders ($\Gamma \gg 10$), the flow is statistically homogeneous in the axial direction. Experimental and numerical simulation data show that the peak
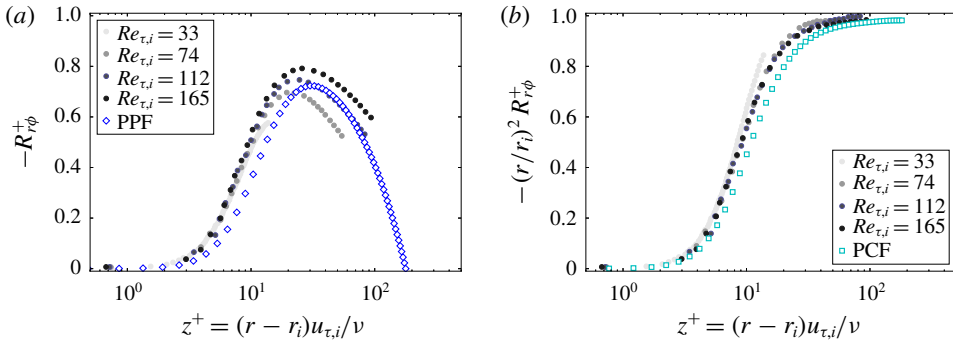
FIGURE 11. Scaling of the Reynolds shear stress for the inner layer. (a) $-R_{r\phi}^+$ versus z^+. The TCF data are from DNS of Dong (2008) with counter-rotating cylinder and $A_t = 0.333$. The turbulent plane channel flow data are from DNS of Moser *et al.* (1999) at $Re_\tau = 180$. (b) $-(r/r_i)^2 R_{r\phi}^+$ versus z^+. The turbulent plane Couette data are from DNS of Kawamura *et al.* (2000) at $Re_\tau = 181$.

Reynolds shear stress location and value are strongly influenced by A_t and $Re_{\tau,i}$. The effect of Π_Ω on the location and value of peak Reynolds shear stress remains to be investigated.

In the inner half of a turbulent TCF, Reynolds shear stress rises sharply from zero to a peak value, then decreases gradually to zero at the outer cylinder. In comparison, in a pressure-driven turbulent channel flow, Reynolds shear stress rises sharply from zero at the wall and decreases almost linearly to zero at the channel centreline (Tennekes & Lumley 1972). The similarities and differences between a turbulent channel flow and a turbulent TCF can be explained by the mean momentum balance equation in the streamwise direction for the two flows

$$0 = \underbrace{\frac{\mathrm{d}^2 U^+}{\mathrm{d}z^{+2}}}_{F_{visc}} + \underbrace{\frac{\mathrm{d}R_{wu}^+}{\mathrm{d}z^+}}_{F_{turb}} + \underbrace{\frac{1}{Re_\tau}}_{F_{pres}} . \quad \text{Turbulent Channel Flow} \quad (4.1a)$$

$$0 = \underbrace{\frac{\mathrm{d}}{\mathrm{d}z^+}\left(\frac{1}{r^*}\frac{\mathrm{d}}{\mathrm{d}z^+}(r^* U_\phi^+)\right)}_{F_{visc}} + \underbrace{\frac{\mathrm{d}R_{r\phi}^+}{\mathrm{d}z^+}}_{F_{turb}} + \underbrace{\frac{A_t}{Re_{\tau,i}}\frac{2R_{r\phi}^+}{r^*}}_{F_{cori}} . \quad \text{Turbulent TCF} \quad (4.1b)$$

In (4.1a), the mean momentum balance for a turbulent channel flow, x is the streamwise direction, and z is the wall-normal direction; $U^+ = U/u_\tau$ denotes the mean streamwise velocity normalized by the friction velocity, $R_{wu}^+ = -\langle wu \rangle/u_\tau^2$ is the kinematic Reynolds shear stress normalized by the square of the friction velocity and the last term comes from the mean pressure force (see Tennekes & Lumley 1972; Pope 2001).

In the outer layer of a turbulent TCF, the turbulent Coriolis force $F_{cori} = 2R_{r\phi}/r$ is a driving force of the flow (see figure 6), similar to the mean pressure gradient $-\mathrm{d}(P/\rho)/\mathrm{d}x = u_\tau^2/\delta$ in a turbulent channel flow. In a turbulent channel flow, the pressure force is a constant, but in a turbulent TCF, F_{cori} is not a constant (see figure 6).

It is observed that in a pressure- or shear-driven turbulent wall-bounded flow, flow transitions to a turbulent state if the friction Reynolds number $Re_\tau = \delta u_\tau/\nu \gtrsim O(100)$.

In a TCF, on the other hand, the friction Reynolds number for the inner half $Re_{\tau,i} = \delta u_{\tau,i}/\nu$ is always larger than for the outer half $Re_{\tau,o} = \delta u_{\tau,o}/\nu$, regardless of the rotation ratio Π_Ω, because $u_{\tau,o}/u_{\tau,i} = (r_i/r_o) = (1 - A_t)/(1 + A_t)$. In a turbulent channel or Couette flow, the channel half-width is typically used as the height of the boundary layer, but flow in a turbulent TCF is not symmetric about the mid-gap, and the border between the inner part and the outer part is not known *a priori*.

For a turbulent TCF with a small Atwood number, $Re_{\tau,i}$ is not much larger than $Re_{\tau,o}$, but at a large Atwood number, the friction Reynolds numbers can be very different. For example, for $Re_{\tau,i} = 1000$, a relatively large Reynolds number, the friction Reynolds number for the outer half will be $Re_{\tau,o} = 52.6$ for $A_t = 0.9$ and $Re_{\tau,o} = 5$ for $A_t = 0.99$. It is reasonable to speculate that for this case the inner part will be highly turbulent, but the outer part cannot sustain a turbulent state and will remain a laminar-like state.

If $Re_{\tau,o}$ is sufficiently high, the scaling of the mean momentum balance equation and the flow structure in the outer half of a TCF gap will be similar to that of the inner half. More specifically, the Reynolds shear stress will have a peak next to the outer cylinder. This peak Reynolds shear stress location will be the centre of a meso-layer (Layer II) for the outer half. The Reynolds shear stress peak near the outer cylinder will be smaller than that near the inner cylinder, and the peak location and peak value depend on the Reynolds number, the geometry Atwood number and perhaps also the rotation ratio as well.

The effect of the rotation ratio Π_Ω on the layer structure and multiscaling analysis of the mean momentum balance equation is not clear at this stage. However, the rotation ratio Π_Ω appears only in the boundary conditions, and is not directly involved in the mean momentum balance equation.

Analysing a Nusselt-style non-dimensional angular velocity flux Nu_ω, Van Gils *et al.* (2012) found that the angular velocity transfer is affected by the cylinder rotation ratio. For a gap with $\Pi_r = 0.716$ or $A_t = 0.165$, Van Gils *et al.* (2012) observed a very pronounced maximum of Nu_ω at $\Pi_\Omega \approx -3$, indicating an optimal angular velocity transport from the inner to the outer cylinder at that angular velocity ratio. The optimal number was refined by Huisman *et al.* (2014) to be $\Pi_\Omega = -2.78$. Ostilla-Mónico *et al.* (2014) investigated the effect of radius ratio on the optimal Taylor–Couette flow, and defined two regimes: a co- and weakly counter-rotating regime, and a strongly counter-rotating regime. Grossmann *et al.* (2016) have shown that the angular velocity profile and flow structures in the bulk of a TCF are strongly influenced by the rotation ratio. As an issue for future research on TCF, they pointed out that a rigorous theoretical understanding of the dependence of an optimal rotation ratio and the gap radius ratio is still missing.

Due to the limitations on the available DNS data on TCF with different Π_Ω, the effect of the rotation ratio on the layer structure is not explored in the present work. It will be very interesting to study the effect of Π_Ω on the distribution of the mean azimuthal velocity U_ϕ and the angular momentum rU_ϕ. It will also be very interesting to study the effect of Π_Ω on the distribution of the Reynolds shear stress $R_{r\phi}$ and the turbulent Coriolis force $2R_{r\phi}/r$. Systematic DNS studies are required. For a TCF with fixed A_t, one could perform a series of simulations at the same $Re_{\tau,i}$ but with different Π_Ω, covering both co-rotating and counter-rotating conditions.

5. Summary

The present work investigated the properties of the mean momentum balance equation for a fully turbulent TCF, and in particular the MMB equation in the

azimuthal ϕ direction. The integrated MMB-ϕ equation confirms that the sum of the moment (or torque) from the viscous shear stress and the Reynolds shear stress is a constant, as was first found by Townsend (1980) and Eckhardt *et al.* (2007). At a sufficiently high Reynolds number, the viscous shear stress is negligible in the core of a turbulent TCF, and the Reynolds shear stress can be approximated as $|R_{r\phi}| \approx (r_i/r)^2 u_{\tau,i}^2$. It is found that the peak Reynolds shear stress location always occurs near the inner cylinder, and it is strongly influenced by the geometry Atwood number A_t and the Reynolds number. The peak Reynolds shear stress location moves closer to the inner cylinder with increasing A_t, and also moves closer to the inner cylinder as the Reynolds number increases. For a fixed A_t, the dependence of the peak Reynolds shear stress location on the Reynolds number is very similar to that in a pressure-driven turbulent channel flow, that is, the peak Reynolds shear location is a meso length scale.

The MMB-ϕ equation is rearranged and integrated to obtain an analytical solution for the global integral of the turbulent Coriolis force. The analytical solution is verified by the DNS studies. It is found that the global integral of the turbulent Coriolis force depends on A_t, Π_Ω, $Re_{\tau,i}$ and $U_{\phi,i}^+$. At the small-gap limit ($A_t \to 0$), the global integral approaches zero $\int_{r_i}^{r_o}(2R_{r\phi}^+/r)\,\mathrm{d}r \to 0$ or $\int_{r_i}^{r_o}(2R_{r\phi}/r)\,\mathrm{d}r \to 0$. In other words, the turbulent TCF at the small-gap limit approaches the turbulent plane Couette flow. At the large-gap limit ($A_t \to 1$), the global integral approaches $\int_{r_i}^{r_o}(2R_{r\phi}^+/r)\,\mathrm{d}r \to -1$ or $\int_{r_i}^{r_o}(2R_{r\phi}/r)\,\mathrm{d}r \to -u_{\tau,i}^2$. At high Reynolds numbers, the global integral of the turbulent Coriolis force is only weakly influenced by the rotation ratio Π_Ω. The effect of the rotation ratio Π_Ω also becomes smaller for $A_t \to 0$.

A three-layer structure is proposed for the inner part of a turbulent TCF, based on the characteristics of force balance in the MMB-ϕ equation: an inner Layer I, a meso Layer II and an outer Layer III. In the inner layer, the force balance is between the viscous force and the Reynolds shear force. In the outer layer, the force balance is between the turbulent Coriolis force and the Reynolds shear force. In the meso-layer, all three forces contribute to the force balance. A three-layer structure will also emerge for the outer part of the TCF gap if $Re_{\tau,o}$ is sufficiently high.

The similarities and differences between a turbulent TCF and a pressure-driven turbulent channel flow are elucidated. The turbulent Coriolis force plays a role similar to that of the pressure force in a turbulent channel flow. However, the pressure force in a fully developed channel flow is a constant, but the turbulent Coriolis force in a turbulent TCF varies in the radial (or wall-normal) direction.

An outer scaling is developed for the outer layer in a fully developed turbulent TCF. In the outer layer, the TCF gap half-width δ is proposed as a proper length scale for the spatial variation in the radial direction $\mathrm{d}r$. A proper length scale for r in the turbulent Coriolis force is the TCF mid-gap location $r_{ctr} = 0.5(r_i + r_o)$. The friction velocity $u_{\tau,i}$ is proposed as a velocity scale for the mean azimuthal velocity, and $u_{\tau,i}^2$ is proposed as a scale for the kinematic Reynolds shear stress. Two non-dimensional numbers emerge from the outer-scaled MMB-ϕ equation: a friction Reynolds number $Re_{\tau,i}$ and a geometry Atwood number A_t.

An inner scaling is developed for the inner Layer I of a fully developed turbulent TCF. In Layer I, the viscous length scale $\nu/u_{\tau,i}$ is proposed as a length scale for the spatial variation in the radial direction $\mathrm{d}r$. Friction velocity $u_{\tau,i}$ is used to scale the mean azimuthal velocity and the kinematic Reynolds shear stress.

The inner scaling and outer scaling for a turbulent TCF are similar to those in a pressure-driven turbulent channel flow, as summarized in table 3. The characteristic scales for length, velocity and Reynolds shear stress are also listed in table 3.

	Taylor–Couette flow	Turbulent channel flow
MMB	$0 = \nu \left\{ \dfrac{d^2 U_\phi}{dr^2} + \dfrac{1}{r}\dfrac{dU_\phi}{dr} - \dfrac{U_\phi}{r^2} \right\} + \dfrac{dR_{r\phi}}{dr} + \dfrac{2R_{r\phi}}{r}$	$0 = \nu \dfrac{d^2 U}{dz^2} + \dfrac{dR_{wu}}{dz} + \dfrac{u_\tau^2}{\delta}$
Inner scaling	$z^+ = \dfrac{r - r_i}{\nu/u_{\tau,i}};\ r^* = \dfrac{r}{r_{ctr}};\ U_\phi^+ = \dfrac{U_\phi}{u_{\tau,i}};\ R_{r\phi}^+ = \dfrac{R_{r\phi}}{u_{\tau,i}^2}$ $0 = \dfrac{d}{dz^+}\left(\dfrac{1}{r^*}\dfrac{d}{dz^+}(r^* U_\phi^+) \right) + \dfrac{dR_{r\phi}^+}{dz^+} + \dfrac{A_t}{Re_{\tau,i}}\dfrac{2R_{r\phi}^+}{r^*}$	$z^+ = \dfrac{z}{\nu/u_\tau};\ U^+ = \dfrac{U}{u_\tau};\ R_{wu}^+ = \dfrac{R_{wu}}{u_\tau^2}$ $0 = \dfrac{d^2 U^+}{d(z^+)^2} + \dfrac{dR_{wu}^+}{dz^+} + \dfrac{1}{Re_\tau}$
Outer scaling	$z^- = \dfrac{r - r_i}{\delta};\ r^* = \dfrac{r}{r_{ctr}};\ U_\phi^+ = \dfrac{U_\phi}{u_{\tau,i}};\ R_{r\phi}^+ = \dfrac{R_{r\phi}}{u_{\tau,i}^2}$ $0 = \dfrac{1}{Re_{\tau,i}}\dfrac{d}{dz^-}\left(\dfrac{1}{r^*}\dfrac{d}{dz^-}(r^* U_\phi^+) \right) + \dfrac{dR_{r\phi}^+}{dz^-} + A_t\dfrac{2R_{r\phi}^+}{r^*}$	$z^- = \dfrac{z}{\delta};\ U^+ = \dfrac{U}{u_\tau};\ R_{wu}^+ = \dfrac{R_{wu}}{u_\tau^2}$ $0 = \dfrac{1}{Re_\tau}\dfrac{d^2 U^+}{d(z^-)^2} + \dfrac{dR_{wu}^+}{dz^-} + 1$

TABLE 3. Comparison of inner scaling and outer scaling for the mean momentum balance equation in the streamwise direction for a turbulent Taylor–Couette flow and a turbulent channel flow. For the turbulent channel flow, x is the streamwise direction and z is the wall-normal direction. U is the mean streamwise velocity, and R_{wu} is the kinematic Reynolds shear stress. Mean pressure gradient is $-d(P/\rho)/dx = u_\tau^2/\delta$ (see Tennekes & Lumley 1972; Pope 2001).

The proposed inner scaling and outer scaling are verified against available DNS data of the mean azimuthal velocity U_ϕ and Reynolds shear stress $R_{r\phi}$. The currently available DNS data are still limited in the parameter space of A_t, Π_Ω and $Re_{\tau,i}$, and in particular, the Reynolds number $Re_{\tau,o}$ is in general too small to establish a three-layer structure in the outer part. More DNS simulations are required to check the validity of the analysis.

TCFs are found in many and varied applications and fields of research. While experimental and theoretical work over the last century has offered considerable insights and data, many questions remain unanswered. The present paper demonstrates a methodology that is shown to be applicable to turbulent flow under different driving mechanisms and geometries. In specific, the present work proposed a three-layer structure, and inner and outer scalings, opening up a pathway for future work on the understanding of the underlying physics in a turbulent TCF.

Acknowledgements

Declaration of interests

The authors report no conflict of interest.

Appendix A. Geometry Atwood number

In studies of Rayleigh–Taylor instability (Glimm *et al.* 2001; Livescu *et al.* 2009; Wei & Livescu 2012), an Atwood number is defined to characterize the density

difference between two fluids

$$A_\rho \stackrel{\text{def}}{=} \frac{\rho_{heavy} - \rho_{light}}{\rho_{heavy} + \rho_{light}}, \tag{A 1}$$

where ρ_{heavy} is the density of the heavy fluid, and ρ_{light} is the density of the light fluid; A_ρ, bounded between 0 and 1, is found to be a very important parameter in the analysis of the Rayleigh–Taylor instability. In the present work, A_t is a non-dimensional ratio of the cylinder radii, and is called the geometry Atwood number. Like the Atwood number in Rayleigh–Taylor instability, the geometry Atwood number is bounded between $0 \leqslant A_t \leqslant 1$

$$A_t \to 0 \quad \text{if } r_i \to r_o; \tag{A 2a}$$
$$A_t \to 1 \quad \text{if } r_i \ll r_o. \tag{A 2b}$$

Appendix B. Viscous force in the MMB-ϕ equation

The viscous force term in (2.6*b*) can also be written in the following forms:

$$F_{visc} = \nu \frac{\mathrm{d}}{\mathrm{d}r} \left(\frac{1}{r} \frac{\mathrm{d}}{\mathrm{d}r} (rU_\phi) \right) \tag{B 1a}$$

$$= \nu \frac{\mathrm{d}}{\mathrm{d}r} \left(\frac{\mathrm{d}U_\phi}{\mathrm{d}r} + \frac{U_\phi}{r} \right) \tag{B 1b}$$

$$= \frac{1}{r^2} \nu \frac{\mathrm{d}}{\mathrm{d}r} \left(r^2 \left(\frac{\mathrm{d}U_\phi}{\mathrm{d}r} - \frac{U_\phi}{r} \right) \right). \tag{B 1c}$$

In (B 1*a*), rU_ϕ is the angular momentum. In (B 1*c*), $\nu(\mathrm{d}U_\phi/\mathrm{d}r - U_\phi/r)$ is the viscous shear stress.

REFERENCES

ABE, H., KAWAMURA, H. & MATSUO, Y. 2001 Direct numerical simulation of a fully developed turbulent channel flow with respect to the Reynolds number dependence. *Trans. ASME J. Fluids Engng* **123** (2), 382–393.

AFZAL, N. 1982 Fully developed turbulent flow in a pipe: an intermediate layer. *Arch. Appl. Mech.* **52** (6), 355–377.

ANDERECK, C. D., LIU, S. S. & SWINNEY, H. L. 1986 Flow regimes in a circular Couette system with independently rotating cylinders. *J. Fluid Mech.* **164**, 155–183.

BRAUCKMANN, H. J. & ECKHARDT, B. 2013 Direct numerical simulations of local and global torque in Taylor–Couette flow up to $Re = 30\,000$. *J. Fluid Mech.* **718**, 398–427.

CHOUIPPE, A., CLIMENT, E., LEGENDRE, D. & GABILLET, C. 2014 Numerical simulation of bubble dispersion in turbulent Taylor–Couette flow. *Phys. Fluids* **26** (4), 043304.

COUETTE, M. 1890 Études sur le frottement des liquides. *Ann. Chim. Phys.* **21**, 433.

DONG, S. 2007 Direct numerical simulation of turbulent Taylor–Couette flow. *J. Fluid Mech.* **587**, 373–393.

DONG, S. 2008 Turbulent flow between counter-rotating concentric cylinders: a direct numerical simulation study. *J. Fluid Mech.* **615**, 371–399.

DONNELLY, R. J. 1991 Taylor–Couette flow: the early days. *Phys. Today* **44** (11), 32–39.

DUBRULLE, B., DAUCHOT, O., DAVIAUD, F., LONGARETTI, P.-Y., RICHARD, D. & ZAHN, J.-P. 2005 Stability and turbulent transport in Taylor–Couette flow from analysis of experimental data. *Phys. Fluids* **17** (9), 095103.

ECKHARDT, B., GROSSMANN, S. & LOHSE, D. 2007 Torque scaling in turbulent Taylor–Couette flow between independently rotating cylinders. *J. Fluid Mech.* **581**, 221–250.

FARDIN, M. A., PERGE, C. & TABERLET, N. 2014 'The hydrogen atom of fluid dynamics' – introduction to the Taylor–Couette flow for soft matter scientists. *Soft Matt.* **10** (20), 3523–3535.

FIFE, P. 2006 Scaling approaches to steady wall-induced turbulence. http://www.math.utah.edu/~fife/revarticle.pdf.

FIFE, P., KLEWICKI, J., MCMURTRY, P. & WEI, T. 2005 Multiscaling in the presence of indeterminacy: wall-induced turbulence. *Multiscale Model. Simul.* **4** (3), 936–959.

VAN GILS, D. P. M., BRUGGERT, G. W., LATHROP, D. P., SUN, C. & LOHSE, D. 2011 The Twente turbulent Taylor–Couette (T3C) facility: strongly turbulent (multiphase) flow between two independently rotating cylinders. *Rev. Sci. Instrum.* **82** (2), 025105.

GLIMM, J., GROVE, J. W., LI, X. L., OH, W. & SHARP, D. H. 2001 A critical analysis of Rayleigh–Taylor growth rates. *J. Comput. Phys.* **169** (2), 652–677.

GROSSMANN, S., LOHSE, D. & SUN, C. 2016 High–Reynolds number Taylor–Couette turbulence. *Annu. Rev. Fluid Mech.* **48**, 53–80.

HUISMAN, S. G., VAN D VEEN, R. C., SUN, C. & LOHSE, D. 2014 Multiple states in highly turbulent Taylor–Couette flow. *Nat. Commun.* **5**, 3820.

KAWAMURA, H., ABE, H. & SHINGAI, K. 2000 DNS of turbulence and heat transport in a channel flow with different Reynolds and Prandtl numbers and boundary conditions. *Turbulence, Heat and Mass Transfer* **3**, 15–32.

KLEWICKI, J., FIFE, P., WEI, T. & MCMURTRY, P. 2007 A physical model of the turbulent boundary layer consonant with mean momentum balance structure. *Phil. Trans. R. Soc. Lond.* A **365** (1852), 823–840.

LANDAU, L. D. & LIFSHITZ, E. M. 1987 *Fluid Mechanics*. Pergamon Press.

LEE, M. & MOSER, R. D. 2015 Direct numerical simulation of turbulent channel flow up to $Re_\tau = 5200$. *J. Fluid Mech.* **774**, 395–415.

LIVESCU, D., RISTORCELLI, J. R., GORE, R. A., DEAN, S. H., CABOT, W. H. & COOK, A. W. 2009 High-Reynolds number Rayleigh–Taylor turbulence. *J. Turbul.* **10**, N13.

LONG, R. R. & CHEN, T.-C. 1981 Experimental evidence for the existence of the 'mesolayer' in turbulent systems. *J. Fluid Mech.* **105**, 19–59.

MALLOCK, A. 1896 Experiments on fluid viscosity. *Phil. Trans. R. Soc. Lond.* A **187**, 41–56.

MARTÍNEZ-ARIAS, B., PEIXINHO, J., CRUMEYROLLE, O. & MUTABAZI, I. 2014 Effect of the number of vortices on the torque scaling in Taylor–Couette flow. *J. Fluid Mech.* **748**, 756–767.

MERBOLD, S., BRAUCKMANN, H. J. & EGBERS, C. 2013 Torque measurements and numerical determination in differentially rotating wide gap Taylor–Couette flow. *Phys. Rev.* E **87** (2), 023014.

MOSER, R. D., KIM, J. & MANSOUR, N. N. 1999 Direct numerical simulation of turbulent channel flow up to $Re_\tau = 590$. *Phys. Fluids* **11** (4), 943–945.

OSTILLA-MÓNICO, R., HUISMAN, S. G., JANNINK, T. J. G., VAN GILS, D. P. M., VERZICCO, R., GROSSMANN, S., SUN, C. & LOHSE, D. 2014 Optimal Taylor–Couette flow: radius ratio dependence. *J. Fluid Mech.* **747**, 1–29.

OSTILLA-MÓNICO, R., STEVENS, R. J. A. M., GROSSMANN, S., VERZICCO, R. & LOHSE, D. 2013 Optimal Taylor–Couette flow: direct numerical simulations. *J. Fluid Mech.* **719**, 14–46.

OSTILLA-MÓNICO, R., VERZICCO, R. & LOHSE, D. 2015 Effects of the computational domain size on direct numerical simulations of Taylor–Couette turbulence with stationary outer cylinder. *Phys. Fluids* **27** (2), 025110.

PIROZZOLI, S., BERNARDINI, M. & ORLANDI, P. 2016 Passive scalars in turbulent channel flow at high Reynolds number. *J. Fluid Mech.* **788**, 614–639.

PIRRO, D. & QUADRIO, M. 2008 Direct numerical simulation of turbulent Taylor–Couette flow. *Eur. J. Mech.* (B/Fluids) **27** (5), 552–566.

POPE, S. B. 2001 *Turbulent Flows*. Cambridge University Press.

RAVELET, F., DELFOS, R. & WESTERWEEL, J. 2010 Influence of global rotation and Reynolds number on the large-scale features of a turbulent Taylor–Couette flow. *Phys. Fluids* **22** (5), 055103.

SCHLICHTING, H. & GERSTEN, K. 2016 *Boundary-Layer Theory*. Springer.

SHINGAI, K., KAWAMURA, H. & MATSUO, Y. 2000 DNS of turbulent Couette flow and its comparison with turbulent Poiseuille flow. In *Advances in Turbulence 8 (Proceedings of the 8th European Turbulence Conference* (ed. C. Dopazo *et al.*), p. 972. CIMNE.

SREENIVASAN, K. R. & SAHAY, A. 1997 The persistence of viscous effects in the overlap region and the mean velocity in turbulent pipe and channel flows. arXiv:physics/9708016.

TANAKA, R., KAWATA, T. & TSUKAHARA, T. 2018 DNS of Taylor–Couette flow between counter-rotating cylinders at small radius ratio. *Int. J. Adv. Eng. Sci. Appl. Math* **10** (2), 159–170.

TAYLOR, G. I. 1936 Fluid friction between rotating cylinders iidistribution of velocity between concentric cylinders when outer one is rotating and inner one is at rest. *Phil. Trans. R. Soc. Lond.* A **157** (892), 565–578.

TENNEKES, H. & LUMLEY, J. L. 1972 *A First Course in Turbulence*. MIT Press.

TOWNSEND, A. A. R. 1980 *The Structure of Turbulent Shear Flow*. Cambridge University Press.

TSUKAHARA, T., KAWAMURA, H. & SHINGAI, K. 2006 DNS of turbulent Couette flow with emphasis on the large-scale structure in the core region. *J. Turbul.* **7**, N19.

VAN GILS, D. P. M., HUISMAN, S. G., GROSSMANN, S., SUN, C. & LOHSE, D. 2012 Optimal Taylor–Couette turbulence. *J. Fluid Mech.* **706**, 118–149.

WEI, T. 2018 Multiscaling analysis of the mean thermal energy balance equation in fully developed turbulent channel flow. *Phys. Rev.* F **3** (9), 094608.

WEI, T. 2019 Multiscaling analysis of buoyancy-driven turbulence in a differentially heated vertical channel. *Phys. Rev.* F **4**, 073502.

WEI, T., FIFE, P., KLEWICKI, J. & MCMURTRY, P. 2005 Properties of the mean momentum balance in turbulent boundary layer, pipe and channel flows. *J. Fluid Mech.* **522**, 303–327.

WEI, T. & LIVESCU, D. 2012 Late-time quadratic growth in single-mode Rayleigh–Taylor instability. *Phys. Rev.* E **86** (4), 046405.

ZIMMERMAN, D. S., TRIANA, S. A. & LATHROP, D. P. 2011 Bi-stability in turbulent, rotating spherical Couette flow. *Phys. Fluids* **23** (6), 065104.